AGU ADVANCING EARTH AND SPACE SCIENCE

JGR Atmospheres

RESEARCH ARTICLE
10.1029/2019JD032088

Key Points:
- The SMART-s algorithm retrieves aerosol particle size distributions and spectral complex index of refraction from about 310 to 800 nm
- We applied the SMART-s algorithm to the AERONET Sun/sky measurements and the retrievals were consistent with the operational products of AERONET
- High spectral resolution of the SMART-s retrievals can provide unique information for atmospheric chemistry, air quality, and climate studies

Correspondence to:
U. Jeong,
ukkyo.jeong@nasa.gov

Citation:
Jeong, U., Tsay, S.-C., Giles, D. M., Holben, B. N., Swap, R. J., Abuhassan, N., & Herman, J. R. (2020). The SMART-s trace gas and aerosol inversions: I. Algorithm theoretical basis for column property retrievals. *Journal of Geophysical Research: Atmospheres*, *125*. https://doi.org/10.1029/2019JD032088

Received 19 NOV 2019
Accepted 10 MAR 2020
Accepted article online 12 MAR 2020

The SMART-s Trace Gas and Aerosol Inversions: I. Algorithm Theoretical Basis for Column Property Retrievals

Ukkyo Jeong[1,2], Si-Chee Tsay[2], David M. Giles[3,2], Brent N. Holben[2], Robert J. Swap[2], Nader Abuhassan[4,2], and Jay R. Herman[4,2]

[1]Earth System Science Interdisciplinary Center, University of MarylandCollege Park, MD, USA, [2]NASA Goddard Space Flight Center, Greenbelt, MD, USA, [3]Science Systems and Applications, Inc., Lanham, MD, USA, [4]Joint Center for Earth Systems Technology, University of Maryland, College Park, MD, USA

Abstract The SMART-s (Spectral Measurements for Atmospheric Radiative Transfer—spectroradiometer) acquires Sun/sky observations for retrieving optimal information on trace gases and aerosols with minimal assumptions. Overall, the algorithm of SMART-s incorporates a series of retrievals, from fundamental quantities (i.e., column abundance of trace gases and aerosol loading) to higher-order geophysical parameters (e.g., aerosol physicochemical properties and vertical profiles), utilizing Sun/sky spectral radiance measurements. This paper describes the theoretical basis for column retrievals of trace gases and aerosols. Associated profile retrievals will be presented in follow-up papers. The current algorithm retrieves the fine/coarse mode of the particle size distribution and spectral complex index of refraction and, thereby, the spectral aerosol single-scattering albedo ω_0. SMART-s retrieval is unique particularly in its high spectral resolution of the complex index of refraction and ω_0 from near-ultraviolet to near-infrared wavelengths, which is pivotal information for atmospheric chemistry, climate and other inversions. We theoretically assessed information content and retrieval accuracy of the algorithm and compared different type of measurements including the Aerosol Robotic Network (AERONET) and standard Pandora. For the same levels of radiometric accuracy, SMART-s measurements provide the most informative aerosol retrievals based on theoretical error analyses. Higher spectral resolution measurements are particularly beneficial for particle size distribution and fine-mode refractive index retrievals. We applied this algorithm to the AERONET Sun/sky measurements at Kanpur, India, in 2016 to assess algorithm consistency. Even with different assumptions and numerical methods for the inversion, SMART-s retrieved aerosol parameters agreed well with the AERONET operational products (e.g., absolute mean bias errors less than 0.01 for ω_0).

1. Introduction

Heterogeneous interactions of atmospheric trace gases and aerosols (e.g., Carlton et al., 2009; Meng et al., 1997; Ziemann & Atkinson, 2012), as well as their considerable variability of distribution and transport in spatiotemporal scales (e.g., Ancellet et al., 2016; Jeong et al., 2017), complicate the management of local and regional air quality (e.g., Keyte et al., 2013; Vieno et al., 2014; Zelenyuk et al., 2012). A significant fraction of urban aerosols is originated by secondary particle formation from their precursors (cf. Zhang et al., 2015, and references therein), which induces critical difficulties for aerosol source identification. Moreover, these small-scale interactions also contribute substantial uncertainties to large-scale climate predictions through aerosol direct and indirect effects (cf. IPCC, 2013, and references therein).

Comprehensive and intensive measurements of atmospheric trace gases and aerosols are crucial to enhance our understanding of their role in the local and global Earth-atmosphere system. Thus far, a series of polar-orbing, shortwave hyperspectral sensors, such as the Global Ozone Monitoring Experiment (Burrows et al., 1999), Global Ozone Monitoring Experiment-2 (Munro et al., 2016), SCanning Imaging Absorption spectroMeter for Atmospheric CHartographY (Bovensmann et al., 1999), ozone monitoring instrument (Levelt et al., 2006), and Ozone Mapping and Profiler Suite (Jaross et al., 2014; Seftor et al., 2014) have continued to offer global coverage of atmospheric trace gas and aerosol products. In the near future, the second-generation hyperspectral sensors onboard a constellation network of geostationary satellites will provide even higher spectral/spatiotemporal resolutions of measurements for trace gas and aerosol

Table 1
Spectral Features of the AERONET, Pandora, and SMART-s

Specification	AERONET	Pandora	SMART-s
Wavelength Range	340–1640 nm	270–530 nm	280–820 nm
Spectral Resolution (Full Width Half Maximum)	2 nm at 340 nm 2 nm at 380 nm 10 nm at 440 nm 10 nm at 500 nm 10 nm at 675 nm 10 nm at 870 nm 10 nm at 1020 nm 25 nm at 1640 nm	0.6 nm	1.0 nm
Sampling Resolution	8 discrete channels	0.13 nm	0.26 nm

Note. The channels of the AERONET may vary depending on the version of instruments. Spectral features of the Pandora and SMART-s may also vary slightly for different wavelengths and units.

retrievals over North America (Chance et al., 2019; Zoogman et al., 2017), Asia (Kim et al., 2019), and Europe (Ingmann et al., 2012). Thus, to complement the advances of atmospheric science spaceborne missions, particularly for calibration/validation and innovative research tasks, simultaneous measurements of trace gases and aerosols using in situ instruments from ground-based (e.g., Du et al., 2010; Stockwell et al., 2016; Tsay et al., 2016) and suborbital platforms (e.g., Guyon et al., 2005; McMeeking et al., 2012) can provide valuable information on their generation, transport, and interaction with a high degree of fidelity.

Since the mid-1990s, the NASA has been operating globally distributed ground-based networks including the AERONET (Aerosol Robotic Network; Holben et al., 1998) and Micropulse Lidar Network (Welton et al., 2001), which have been providing critical aerosol and cloud measurements for validation and comparison of satellite products. Recently, the expansion of NASA's Pandora network (e.g., Szykman et al., 2019) has focused on retrieving trace gases (e.g., O_3, NO_2, and HCHO) using its Sun/sky hyperspectral measurements from charge-coupled devices (CCD) and validated/compared them against other instruments for multiple years (Herman et al., 2009, 2015, 2019). However, deriving information on vertical profile of trace gases from the standard Pandora (i.e., wavelengths ranging in 270–530 nm) measurements is challenging due to the lack of information content and other error sources, such as the aerosol models assigned (e.g., Bösch et al., 2018; Chimot et al., 2016; Hong et al., 2017). Wagner et al. (2004) demonstrated that the slant column density (SCD) of the oxygen dimer (O_2–O_2 or O_4) from spectral measurements is sensitive to the aerosol extinction profile even though absolute radiometric calibrations are not required when utilizing the Differential Optical Absorption-Spectroscopy method. In addition, algorithms for retrieving aerosol extinction profiles typically utilize the assumed aerosol optical properties (e.g., phase function or $P(\Theta)$, single-scattering albedo or ω_0), since O_4 SCD measurements are less sensitive to these parameters (e.g., Bösch et al., 2018; Frieß et al., 2006; Irie et al., 2008; Wagner et al., 2004). Thus, the retrieved aerosol extinction profile, together with assumed ω_0 and $P(\Theta)$, is used for retrieving the vertical profile of trace gases (e.g., Bösch et al., 2018; Irie et al., 2011).

Absolute radiometric calibrations of CCD-based instruments are challenging, since it is sensitive to ambient conditions, particularly to temperature; hence, they require specific maintenance (e.g., Sentenac et al., 2003; van Geffen, 2004). However, CCD instruments can measure radiances at thousands of wavelengths simultaneously, which provides information on aerosols and trace gases from single acquisition (e.g., Hansell et al., 2014; Jeong et al., 2018). The SMART-s was originally developed by NASA's Pandora network group as a CCD-based Sun/sky spectroradiometer covering broader wavelengths with lower spectral resolution than standard Pandora instruments (from about 280 to 820 nm, with about 1.0 nm resolution and 3.7 times oversampling). Table 1 compares spectral features of the AERONET, Pandora, and SMART-s.

Even with the lower spectral resolution of SMART-s compared to the Pandora instruments, they provide consistent total column of NO_2 and O_3 products as compared in Figure 1 from similar fitting windows. The measurements of SMART-s and Pandora in this Figure are acquired from the rooftop at NASA Goddard Space Flight Center (GSFC; 38.9925°N, 76.83983°W, 87 m) Building 33 during March 2018.

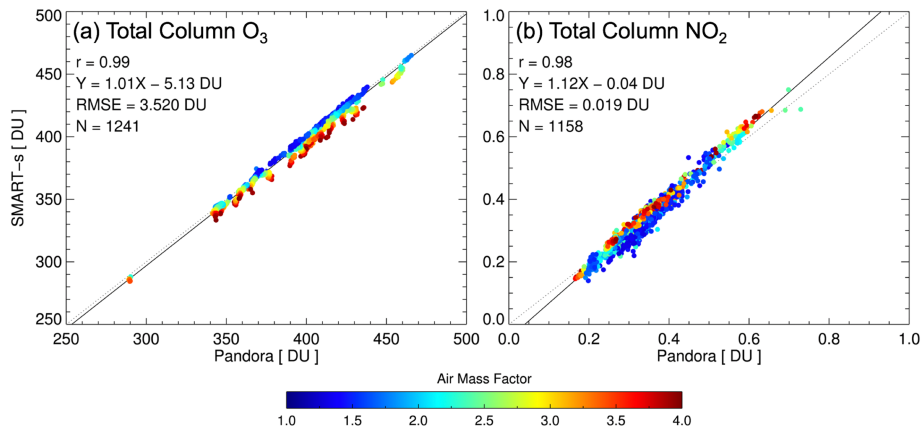

Figure 1. Comparison of total column retrievals of (a) ozone and (b) nitrogen dioxide from the Pandora (*x* axis) and SMART-s (*y* axis) instruments measured at Building 33 of NASA/GSFC during March 2018. The colors of circles represent geometric air mass factor of each retrieval.

Current trace gas retrieval algorithm of the SMART-s used in Figure 1 is similar to the operational method (e.g., Herman 2009 and 2015) except for minor modifications. The colors of circles show geometric air mass factor of each retrieval. The O_3 retrievals of SMART-s show negative biases compared to the Pandora products at large air masses due to stray light contamination in ultraviolet channels (see Figure 1a). However, NO_2 retrievals of both instruments show consistent agreement even at large air masses, since visible channels suffer less from the stray light as shown in Figure 1b. Note that the SMART-s spectral range covers ozone Chappuis band that also can be used for increasing information content of tropospheric ozone, as well as for its total column retrievals. Jeong et al. (2018) reported that well calibrated and maintained SMART-s instrument offers high-spectral resolution retrievals of aerosol optical thickness (τ_{aer}), which are in excellent agreement with those retrieved from the collocated AERONET measurements at available discrete channels. The spectral τ_{aer} is a key constraint of higher-order inversion of aerosol microphysical properties (Dubovik & King, 2000), which are also critical for vertical profile retrievals of aerosols and trace gases.

The retrieval algorithm of SMART-s aims to obtain optimal information on trace gases and aerosols simultaneously with minimal assumptions. The algorithm is comprised of several retrieval steps from basic quantities (i.e., total column amounts of trace gases and aerosols) to higher-order parameters (e.g., aerosol microphysical properties, vertical profiles of aerosols, and trace gases), which are designed to avoid mutual interferences among different parameters (see Figure 2).

After thorough calibration procedures of SMART-s by applying the spectral-Langley-method from the field (Jeong et al., 2018) and spectral characterization/absolute radiometric calibrations in laboratory facilities (Herman et al., 2009, 2015), the total column abundances (TCAs) of trace gases are first retrieved from direct Sun spectral measurements. Then, the spectral τ_{aer} can be derived by subtracting out the absorption optical thickness of trace gases, associated with TCAs from the previous step, using the total spectral optical thickness. Note that the spectral τ_{aer} retrievals at this step are not affected by the type or vertical distribution of aerosols (Jeong et al., 2018). Similar to the AERONET protocol, the combination of TCAs of trace gases, spectral τ_{aer}, and almucantar measurements of sky radiance, the column microphysical and optical properties of aerosols are readily retrieved (e.g., Dubovik & King, 2000). The solar almucantar measurements at this step are likewise not sensitive to the vertical distribution of aerosols (Dubovik et al., 2000). As sketched in Figure 2, the vertical profile of aerosols can be derived by using spectral measurements and SCD of oxygen dimer bands from the solar principal plane, as well as constraints on aerosol retrievals and TCA of trace gases from prior steps. Wavelengths in this step are carefully selected so that they are not sensitive to vertical profiles of trace gases. The final step is to retrieve vertical profiles of trace gases, which are constrained by comprehensive sets of atmospheric conditions including all information on aerosols and trace gases from prior steps. Merits of SMART-s trace gas and aerosol retrieval algorithm are highlighted below:

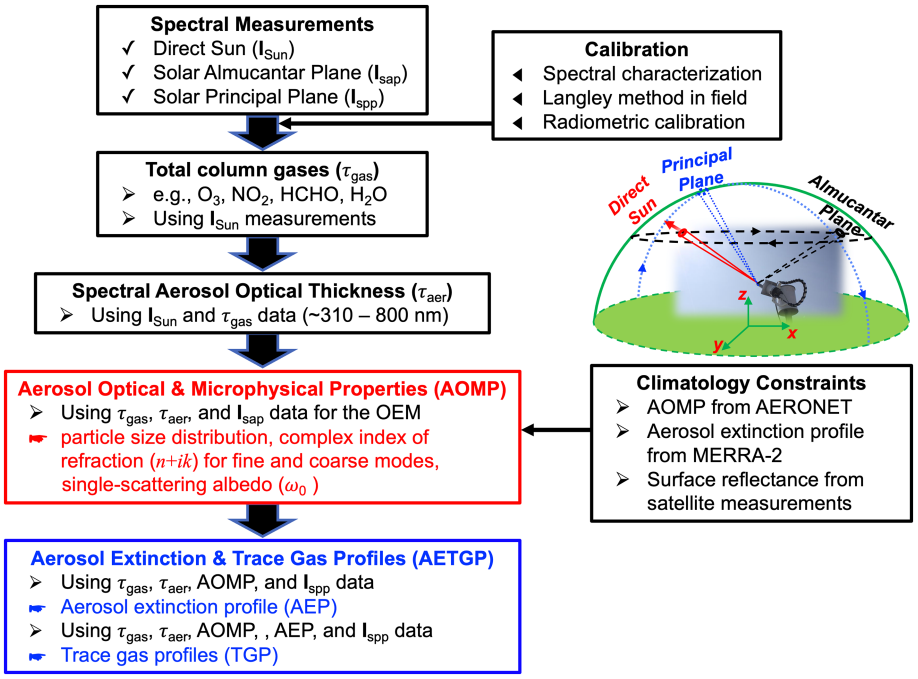

Figure 2. Flowchart of the trace gas and aerosol retrieval algorithms of the SMART-s. Algorithms for the black steps are developed and validated, the step with red color is algorithm presented in this study, and steps with blue color indicate the algorithms and products will be reported in a follow-up paper.

1. It directly measures spectral τ_{aer} within spectral coverage of a spectrometer, thus can provide τ_{aer} using any fitting window for vertical profile retrieval of trace gases without any interpolation and/or extrapolation.
2. Inversion products of aerosol column properties including particle size distribution (PSD) and spectral complex index of refraction are directly used for retrievals of vertical profile of aerosols and trace gases which minimize assumptions on aerosol models.
3. An optimal estimation method (OEM; Rodgers, 2000) based algorithm with a well-tested linearized radiative transfer model (see below) provides reliable error estimates/analyses, which is valuable for relevant studies using the retrievals (e.g., data assimilations).

This paper describes the algorithm theoretical basis for retrieving aerosol properties, followed by TCA of trace gases (Herman et al., 2009, 2015, 2019) and spectral τ_{aer} (Jeong et al., 2018) retrievals, using direct Sun and solar almucantar measurements. The absolute radiometric calibration of sky-scan measurements is successfully finished by utilizing NASA/Goddard space flight calibration facility. Section 2 describes theoretical basis of the inversion method, and section 3 shows error estimation method and information content of the retrievals. In section 4, we applied the developed algorithm to AERONET's almucantar measurement at Kanpur (India), then compared the results with operational AERONET inversion products to check consistency. In Appendix A, we reported details of the estimated retrieval error for different radiometric calibration accuracy, spectral resolution, and aerosol type. Appendix B describes the estimated degrees of freedom for signal, and in Appendix C, we checked the algorithm consistency at another site (Seoul, South Korea).

2. Algorithm Theoretical Basis and Implementation

Based on the Bayes's theorem (Bayes & Price, 1763), the OEM finds a probability distribution of a physical state (state vector; $\mathbf{x}$) based on prior knowledge of conditions that may be related to the $\mathbf{x}$ (a priori; mean state of $\mathbf{x}_a$ with covariance of $\mathbf{S}_a$), as well as a set of measurements ($\mathbf{y}$) with uncertainties ($\mathbf{S}_a$). The SMART-s aerosol inversion algorithm finds a probability distribution of aerosol column properties (e.g., particle size distribution and complex refractive indices) based on various sources of a priori data and Sun/sky measurements. It iteratively finds an optimum state of $\mathbf{x}$ that minimizes following cost function (cf. Rodgers, 2000 for more details):

$$\chi^2 = \left\| \mathbf{S}_\varepsilon^{-\frac{1}{2}}[\mathbf{y} - \mathbf{F}(\mathbf{x})] \right\|_2^2 + \left\| \mathbf{S}_a^{-\frac{1}{2}}(\mathbf{x} - \mathbf{x}_a) \right\|_2^2, \tag{1}$$

where χ is the cost function, $\mathbf{S}_a$ is the error covariance matrix of measurements, and $\mathbf{y}$ is the measurement vector. $\mathbf{F}(\mathbf{x})$ is the forward model that generates theoretical $\mathbf{y}$ by using the $\mathbf{x}$ as input data. For a linear problem, the forward model can be expressed as $\mathbf{Kx}$, where $\mathbf{K}$ is the weighting function matrix of which the elements are partial derivatives of each measurement with respect to the state vector. $\mathbf{S}_a$ and $\mathbf{x}_a$ is the covariance and mean state vector of a priori information, respectively. An accurate forward model using an ideal state of $\mathbf{x}$ simulates Sun/sky measurements that are close to the measurement ($\mathbf{y}$), thus minimizes the first term of right-hand-side of equation (1). At the same time, minimizing the second term of right-hand side of equation (1) forces $\mathbf{x}$ to be constrained to the $\mathbf{x}_a$ weighted by $\mathbf{S}_a$. By using those two constraints, the algorithm chooses the most realistic state among multiple solutions, thus suffers less from local minimum and/or unphysical solutions.

The measurement vector of the SMART-s aerosol algorithm consists of sky radiance measurements at solar almucantar plane, as well as spectral τ_{aer} from the direct Sun measurements like AERONET (Dubovik & King, 2000). Largely due to the temperature sensitivity of the spectrometer, the retrieval error of τ_{aer} from SMART-s is estimated to be about 0.02 (Jeong et al., 2018), slightly larger than that of AERONET. The AERONET uncertainty in the field measurements is 0.01 for nonultraviolet (non-UV) wavelengths and 0.02 for UV wavelengths (Eck et al., 1999; Giles et al., 2019; Holben et al., 1998). For radiometric calibration, NASA/GSFC Calibration Facility provides well-maintained NIST-traceable light sources with an accuracy of 1%–2%. Based on the recently finished laboratory calibration using the light source, we estimate radiometric accuracy of SMART-s to be better than 3% (including uncertainties in the light source and instrument stability), which is at a similar level of recent AERONET calibrations. Detailed radiometric calibration procedures and results will be described in a follow-up paper.

For the radiative transfer (RT) calculations, we utilized VLIDORT (linearized pseudo-spherical vector Discrete Ordinate Radiative Transfer) code, which provides analytic weighting functions with respect to the aerosol microphysical parameters and vertical profiles (Spurr, 2006; Spurr et al., 2012; Spurr & Christi, 2014). An analytic function of lognormal-bimodal distribution, which is a function of two parameters for each lognormal mode (mean radius and geometric standard deviation) and number fraction of fine mode (F_{num}), is used to represent the number size distribution of aerosols as follows (Spurr et al., 2012):

$$n(r) = \frac{F_{\mathrm{num}}}{\sqrt{2\pi}\ln\sigma_{\mathrm{f}}}\frac{1}{r_{\mathrm{f}}}\exp\left[-\frac{1}{2}\left(\frac{\ln r - \ln r_{\mathrm{f}}}{\ln\sigma_{\mathrm{f}}}\right)^2\right] + \frac{(1-F_{\mathrm{num}})}{\sqrt{2\pi}\ln\sigma_{\mathrm{c}}}\frac{1}{r_{\mathrm{c}}}\exp\left[-\frac{1}{2}\left(\frac{\ln r - \ln r_{\mathrm{c}}}{\ln\sigma_{\mathrm{c}}}\right)^2\right], \tag{2}$$

where r_{f} and σ_{f} are the mean radius and geometric standard deviation of fine mode, respectively, and r_{c} and σ_{c} are those for coarse mode. We obtain climatology of these parameters by converting the $n(r)$ to volume-size distribution then iteratively fit it to 22 radius nodes of the AERONET retrieval. Those values are utilized for $\mathbf{S}_a$ and $\mathbf{x}_a$ in equation (1). For single-scattering calculations, spherical particles are assumed, but an update for more general shapes (Mishchenko et al., 2010; Spurr et al., 2012; Yang et al., 2007) is currently underway. Note that error analysis and retrievals in this study assume aerosols are spherical. Use of nonspherical particles may have different results. At this step of the algorithm in Figure 2, we assume an extinction profile of the aerosols with Gaussian shape for simplicity, since solar almucantar plane radiances are not meaningfully sensitive to the vertical profile of the aerosols. The Gaussian shape of the vertical extinction profile can be expressed as follows (Spurr & Christi, 2014):

$$A(z) = W\frac{e^{-h(z-z_{\mathrm{p}})}}{\left[1+e^{-h(z-z_{\mathrm{p}})}\right]^2}, \tag{3}$$

where $A(z)$ is the extinction profile of aerosols and the constant W normalizes total aerosol extinction. z_{p} is the peak height and h is related to the vertical dispersion of the Gaussian profile shape. We use z_{p} and h climatology converted from aerosol profiles of reanalysis data (e.g., Modern-Era Retrospective analysis for Research and Applications, Version 2; Gelaro et al., 2017) for the a priori constraints. In this study, we assumed the surface is a Lambertian reflector, where a priori data are obtained from merged satellite

Table 2
Parameters and Their Indices, A Priori Sources of State Vector for SMART-s Aerosol Inversion Algorithm

Parameter index	Parameter	Sources of a priori
1	Mean radius of fine mode (r_f)	AERONET
2	Geometric standard deviation of fine mode (σ_f)	AERONET
3	Mean radius of coarse mode (r_c)	AERONET
4	Geometric standard deviation of coarse mode (σ_c)	AERONET
5	Number fine-mode fraction (F_{num})	AERONET
6	Peak height of the aerosol (z_p)	[a]MERRA-2
7	Half width of the aerosol layer (h)	[a]MERRA-2
Next n Wavelengths	Fine-mode real refractive index (n_f)	AERONET
Next n Wavelengths	Coarse-mode real refractive index (n_c)	AERONET
Next n Wavelengths	Fine-mode imaginary refractive index (k_f)	AERONET
Next n Wavelengths	Coarse-mode imaginary refractive index (k_c)	AERONET
Next n Wavelengths	Lambertian surface albedo (ρ)	Merged using multiple satellite sensors

Note. The parameter indices vary depending on the number of wavelengths utilized for the algorithm.
[a]The Modern-Era Retrospective Analysis for Research and Applications Version 2 (MERRA-2).

measurements. Spectral surface reflectance has limited impact on the SMART-s aerosol inversion. The elements of **x** in equation (1), their indices and a priori sources are summarized in Table 2.

Since the spectral measurements for all wavelengths are acquired simultaneously, the SMART-s aerosol retrieval algorithm can adjust the effective spectral resolution for the inversion as needed. Similarly, the operation procedures of SMART-s also can control the angular resolution of the sky radiance field to give the needed information content. Theoretically, an algorithm can extract optimum information from higher spectral and angular (and/or spatial, temporal) resolutions of measurements. However, larger dimension of **y** (thus **F**) in equation (1) increases risk of numerical instability (particularly for the inversion matrix), as well as the increased existence of local minimum. Selection of appropriate spectral/angular resolution for **y** is governed by considering these two aspects. On the angular perspective, we adopt AERONET's almucantar-scan strategy (viewing zenith angle [θ_v] = solar zenith angle [θ_s]; relative azimuth angle [ϕ_r] = 3.0°, 3.5°, 4.0°, 5.0°, 6.0°, 7.0°, 8.0°, 10.0°, 12.0°, 14.0°, 16.0°, 18.0°, 20.0°, 25.0°, 30.0°, 35.0°, 40.0°, 45.0°, 50.0°, 60.0°, 70.0°, 80.0°, 90.0°, 100.0°, 120.0°, 140.0°, 160.0°, 180.0°), which contains information on the aerosol phase function (Nakajima et al., 1983, 1996) and ω_0 (Devaux et al., 1998; Dubovik et al., 1998; Holben et al., 1996), and has been optimized by decades of experience to efficiently extract the necessary information. Another crucial constraint of the OEM is the a priori information. For its extensive temporal and spatial coverage on aerosol information, AERONET provides long-term global climatology of aerosol column properties (e.g., complex index of refraction and particle size distribution) for SMART-s aerosol retrieval algorithm (see Table 2). Figure 3a shows an example of $\mathbf{S}_a$ from AERONET climatology at NASA/GSFC. Figure 3b is the interpolated/extrapolated $\mathbf{S}_a$ from (3a) to the spectral range of SMART-s retrievals (i.e., 330–800 nm, with 10-nm resolution). The number of elements of PSD (r_f, σ_f, r_c, σ_c, and F_{num}) and aerosol layer height (ALH; z_p and h) inside the red square in Figure 3 is a constant value of 7, whereas those of the refractive index and surface albedo are equal to the number of wavelengths utilized. The smoothness constraint of AERONET algorithm for retrievals of index of refraction ($n + ik$: n for real part and k for imaginary part) results in large off-diagonal elements for $\mathbf{S}_a$. These large covariances between different wavelengths also force the SMART-s retrievals of n and k to be spectrally smooth. However, we degraded the constraints of spectral smoothness of n and k by downweighting off-diagonal elements of $\mathbf{S}_a$ (for n and k) to obtain higher degrees of freedom and to capture their specific spectral features. This downweighting also decreases the condition number of the a priori covariance matrix, thus stabilizes calculations of its inversion matrix. Note that the algorithm retrieves complex index of refraction for fine (n_f and k_f) and coarse mode (n_c and k_c) separately, whereas AERONET operational algorithm retrieves single complex index of refraction for both modes ($n + ik$). We use n and k of the AERONET climatology as a priori constraint for both fine and coarse mode of the SMART-s retrievals. Estimated information content of n and k of each mode is described in section 3 and Appendix B. Identical global statistics of the AERONET climatology data are applied to each site as a priori constraints which mostly impact large outliers. However, we utilize minimum constraints of the climatology for retrievals to reduce dependency on sources of the a priori;

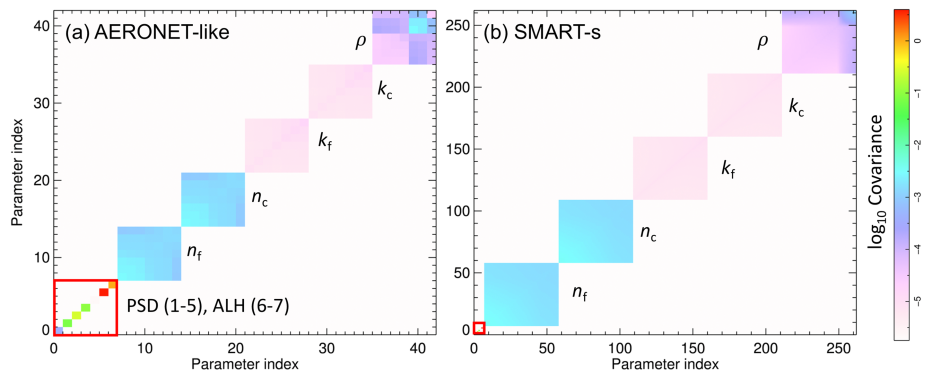

Figure 3. (a) An example of covariance matrix from AERONET aerosol climatology at NASA/GSFC from 1993 to 2019 and (b) interpolated/extrapolated matrix for SMART-s from (a). These data represent the actual statistics and not the scaled values for the inversion. Parameter indices from 1 to 5 denote aerosol particle size distribution (PSD) and 6–7 are aerosol layer height (ALH) parameters. Larger indices are of real (n) and imaginary (k) part refractive indices of fine-(subscript f) and coarse-mode (subscript c) aerosols and spectral surface albedo (ρ).

the algorithm uses 10–100 times larger values of $\mathbf{S}_a$ than actual statistics shown in Figure 3. In our experience, the a priori constraint has negligible impact on typical retrievals but has larger effect on outliers which typically suffer from local minima and/or failure of convergence.

3. Error Analysis

Well-characterized error estimation of an inversion product is very useful for relevant studies. The OEM estimates $\hat{\mathbf{x}}$, the retrieval parameter vector, from the measurements and *a priori* information as follows:

$$\hat{\mathbf{x}} = \mathbf{x}_a + \left(\mathbf{K}^T\mathbf{S}_\epsilon^{-1}\mathbf{K} + \mathbf{S}_a^{-1}\right)^{-1}\mathbf{K}^T\mathbf{S}_\epsilon^{-1}(\mathbf{y} - \mathbf{K}\mathbf{x}_a) = \mathbf{x}_a + \mathbf{A}(\mathbf{x} - \mathbf{x}_a) + \mathbf{G}\epsilon, \tag{4}$$

where $\mathbf{G}$ is the gain matrix ($\partial\hat{\mathbf{x}}/\partial\mathbf{y}$), representing the sensitivity of retrievals to the measurement, and ϵ is the measurement noise. The averaging kernel matrix ($\mathbf{A}$), sensitivity of retrievals to a true state, can be expressed as follows:

$$\mathbf{A} = \mathbf{G}\mathbf{K} = \frac{\partial\hat{\mathbf{x}}}{\partial\mathbf{x}}. \tag{5}$$

Equation (4) also characterizes how the retrieval ($\hat{\mathbf{x}}$) is biased from the true state ($\mathbf{x}$) by an averaging kernel ($\mathbf{A}$) and measurement error (ϵ), which provides theoretical estimate of retrieval errors (e.g., Jeong et al., 2016; Rodgers, 1990, 2000).

We estimated accuracy and information content of the aerosol inversion products from SMART-s measurements for three major aerosol types (i.e., smoke, sulfate, and dust). Table 3 summarized parameters of the aerosol models which are derived from AERONET climatology (Jeong et al., 2016; Torres et al., 2007) and the Optical Properties of Aerosols and Clouds database (Hess et al., 1998). The parameters of number size distributions in Table 3 are derived by fitting to the AERONET's volume size distribution products. In Table 3, k was determined for ω_0 to have sufficient range (from 0.74 to 0.99 at 440 nm). The volume size distributions of each aerosol type converted from the size parameters in Table 3 are compared in Figure 4.

Table 3
The Number Size Distribution Parameters, Complex Index of Refraction ($n + ik$), and Single-Scattering Albedo (ω_0) at 440 nm for Sulfate, Smoke, and Dust Aerosol Model Used in This Study

Aerosol type	r_f	σ_f	r_c	σ_c	F_{num}	n	k	ω_0 (440 nm)
Sulfate	0.088	1.499	0.509	2.160	0.999596	1.40	0.001	0.99
Smoke	0.080	1.492	0.705	2.075	0.999795	1.50	0.010	0.93
Dust	0.052	1.697	0.670	1.806	0.995650	1.55	0.020	0.74

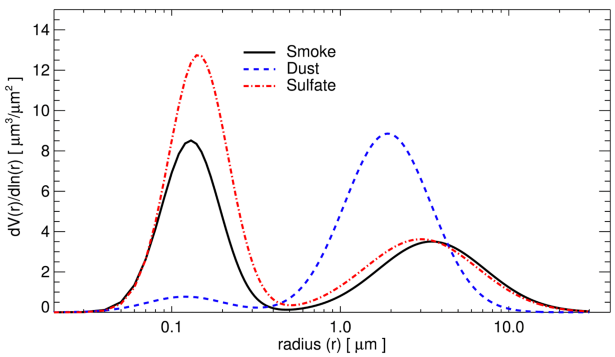

Figure 4. Volume size distribution of smoke (black), dust (blue), and sulfate (red) aerosol type used for sensitivity/error analysis in this study.

AERONET's current operational algorithm is using solar almucantar/hybrid scan measurements at 440, 675, 870, and 1,020 nm. The hybrid sky scan of AERONET combines solar principal and almucantar scan, which provides symmetric sky scanning making it less sensitive to cloud contamination for wider range of solar zenith angles (more details are at https://aeronet.gsfc.nasa.gov/new_web/optical_properties.html). Recently, AERONET extended its sky scan wavelengths to provide aerosol optical properties at more channels. In this study, we used the extended AERONET Sun/sky measurements at Kanpur, India (26.51278°N, 80.23164°E, 123 m) in 2016 as a testbed, which is scanning sky radiances at seven wavelengths (i.e., 380, 440, 500, 675, 870, 1,020, and 1,640 nm). We applied the SMART-s aerosol inversion algorithm to τ_{aer} and solar almucantar radiances from AERONET measurements at the extended wavelengths. (We define resulted retrievals as AERONET-like inversion products hereafter.) An example of **K** for the seven wavelengths of sulfate aerosol with τ_{aer} at 440 nm of 1.0 and θ_s of 60° is shown in Figure 5. Each row of the **K** corresponds to each element of **y** and consists of radiance (28 scan angles × 7 wavelengths) and τ_{aer} (seven wavelengths) measurement components. The elements of columns of **K** correspond to elements of **x** listed in Table 2. We assume sky radiances and τ_{aer} at a wavelength are independent from n, k, and surface albedo at different wavelengths (i.e., weighting functions of **x** with respect to refractive indices and surface albedo at other wavelengths are zero). By definition, the weighting functions of τ_{aer} with respect to vertical profile of aerosols and surface albedo are also zero as shown in Figure 5.

3.1. Retrieval Sensitivity

The averaging kernel matrix (**A**) in equation (5) has been widely used to estimate information content from a set of measurements and inversion method (e.g., Frankenberg et al., 2012; Rodgers, 1990, 1998; Sanghavi et al., 2012; Xu and Wang, 2015). As an example, the array element A_{ij} represents the sensitivity of retrievals at row i to the variables at column j. Therefore, for an inversion of an ideal observing system, a retrieval has no cross correlation so that $\mathbf{A} = \mathbf{I}$, an identity matrix, which is not often the case (Rodgers, 1990). Diagonal elements of **A** ($D_{\mathbf{A}}$) close to one represent a set of measurements and an inversion method that is sufficiently sensitive for an accurate retrieval, whereas off-diagonal elements represent retrieval errors by interference with other parameters or by lack of information content in the measurements. For a typical atmospheric profile algorithm using passive sensors, its vertical information is obtained using the spectral sensitivity to radiances (e.g., ozone molecules at different altitude have different spectral radiance weighting functions) and/or different viewing geometry. However, these spectral radiances and the vertical distribution of atmospheric parameters are not in a one-to-one relationship and are often ill posed, which results in smoothed vertical response function (i.e., low information content in the averaging kernel or row of **A**). For that reason, profile retrievals have been defined as either true state or information poor smoothed profile by the rows of **A** (e.g., Backus & Gilbert, 1970; Menke, 1984; Rodgers, 1990). This approach is reasonable, since a typical derived vertical profile of atmospheric parameters is a smooth function of altitude. That is, when the model resolution is better than or comparable to natural variability, then the smoothed profile can well represent the true state.

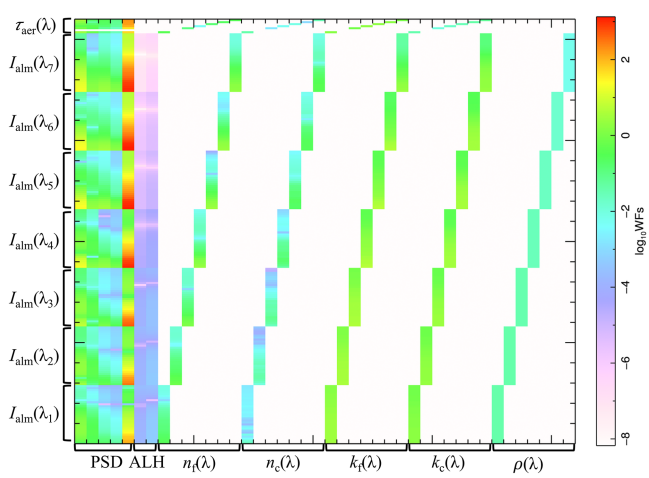

Figure 5. An example of weighting function (WFs) matrix (**K**) for AERONET-like almucantar measurements with seven wavelengths. Each row represents element of state vector, and each column indicates measurement component including spectral sky radiances and aerosol optical thickness. Aerosol type for this calculation is sulfate (fine mode dominated, mostly scattering), with optical thickness at 440 nm of 1.0 and solar zenith angle of 60°.

In the inversion method for the SMART-s aerosol column property algorithm in this study, all state vectors are independent variables; nonzero off-diagonal elements of **A** indicate retrieval errors by interference with other parameters and/or lack of information content. Natural variabilities of the n, k, and ρ are known to be spectrally smooth (see Figure 3), and this spectral smoothness is constrained by the off-diagonal elements of the $\mathbf{S}_a$.

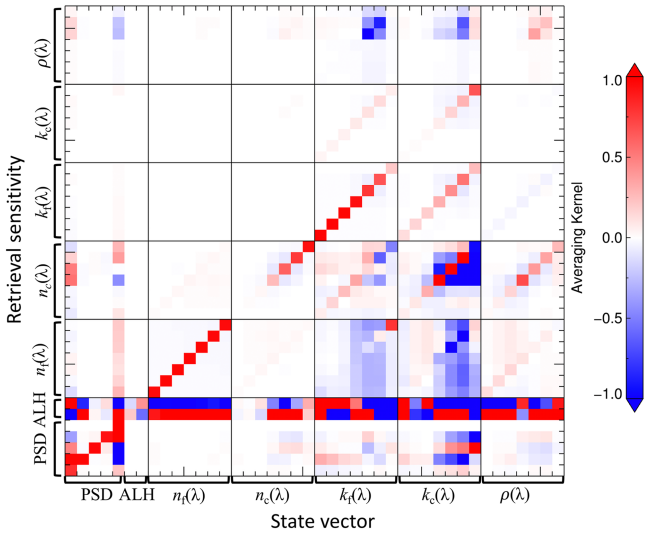

Figure 6. Averaging kernel matrix of smoke aerosol at solar zenith angle of 60° using the AERONET-like solar almucantar measurements (wavelengths at 380, 440, 500, 675, 870, 1,020 and 1,640 nm).

Note that, we downweighted the off-diagonal elements of the $\mathbf{S}_a$ of n and k as described in section 2. Unlike vertical resolutions of profile algorithms, the n, k, and ρ at a wavelength are not affected by these parameters at other wavelengths, thus are better well posed since they only perturb Sun/sky measurements at the corresponding wavelength. Therefore, when their retrieval sensitivity is sufficient, we expect that the spectral resolution of these parameters is high enough to represent true states. Columns of the $\mathbf{A}$ represent response of the inversion to a δ-function perturbation of a true state (Rodgers, 1990).

Figure 6 shows $\mathbf{A}$ for the smoke (fine-mode dominated and moderately absorbing) aerosol at a θ_s of 60° for AERONET-like solar-almucantar measurements. The $D_{\mathbf{A}}$s of PSD parameters (indices of 1–5) show their sufficient retrieval sensitivity from the measurement, which are close to one. Particularly, off-diagonal elements in rows of $\mathbf{A}$ ($R_{\mathbf{A}}$) for the r_f and the F_{num} have small absolute values, which indicate these retrievals are not affected by other parameters. On the contrary, $R_{\mathbf{A}}$s of the r_c, σ_f, and σ_c indicate that their retrievals are affected by the r_f, F_{num}, and k_c (see the $R_{\mathbf{A}}$s of rows 2–4). Due to the predominant sensitivity of F_{num} to the measurement set, it affects all other PSD parameters and the n retrievals, which results in high absolute values of off-diagonal elements in fifth column of $\mathbf{A}$ ($C_{\mathbf{A}}$). As is well recognized, solar-almucantar measurements are not sensitive to vertical profiles of aerosols (e.g., Dubovik et al., 2000; Dubovik & King, 2000), which is reflected in low values of $D_{\mathbf{A}}$ and high absolute values of $R_{\mathbf{A}}$ for the two ALH parameters (see the rows for ALH of $\mathbf{A}$).

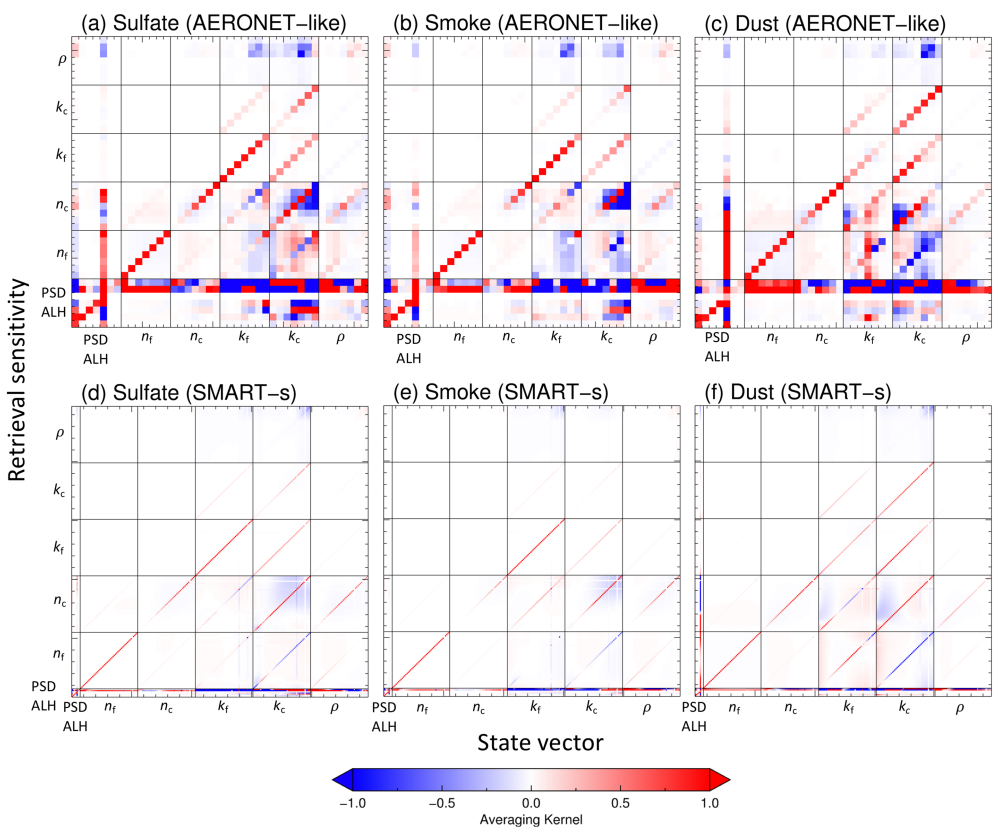

Figure 7. Averaging kernel matrix using the AERONET-like spectral measurements for (a) sulfate, (b) smoke, and (c) dust aerosols at solar zenith angle of 75°. The panels (d)–(f) are averaging kernels for these aerosols but using the SMART-s measurements (from 330 to 800 nm, with a 10-nm resolution).

The vertical profiles of aerosols and trace gases will be retrieved from solar-principal plane scans using retrievals from prior steps (i.e., total column amounts of aerosols and trace gases and aerosol microphysical properties) as described in Figure 2. Since the smoke aerosols are fine-mode dominated type, retrievals of the n_f are more sensitive than n_c (compare the $D_{\mathbf{A}}$s of n_f with n_c in Figure 6). The n_f retrievals are affected by the F_{num} and k, and the n_c retrievals are additionally affected by r_f and surface albedo. However, the $R_{\mathbf{A}}$ of n_f at n_c are negligible and vice versa (see $R_{\mathbf{A}}$ of n_f and n_c in Figure 6), which suggests that the retrieval sensitivities of the n_f and n_c are independent and can be retrieved separately by the SMART-s algorithm. On the contrary, the retrieval of k is less affected by other parameters (i.e., n, PSD, ALH, and ρ), whereas the reciprocal $R_{\mathbf{A}}$ values of the k_f *and* k_c are significant due to correlated measurement sensitivity. The retrieval sensitivity of spectral surface albedo (ρ) is small and affected by the k at near-IR wavelengths (870 and 1,020 nm), whereas the $D_{\mathbf{A}}$ and $R_{\mathbf{A}}$ values at other wavelengths were negligible. In the current algorithm, we limited the retrieval range of θ_s up to 75° to minimize the effects of surface reflectance at high θ_s and θ_v. Additional polarization measurements and/or consideration of more sophisticated bidirectional surface reflectance effects can improve the information content and extend the retrieval range, which will be investigated in a future algorithm.

Panels in Figure 7 are similar to the plot in Figure 6 but compare **A**s at higher θ_s (75°) for different type of aerosols and spectral measurements. The upper three panels of Figure 7 are **A**s for (a) sulfate, (b) smoke, and (c) dust aerosols using the AERONET's seven solar almucantar wavelengths, and lower panels (d to f) are those for the SMART-s wavelengths (from 330 to 800 nm with a 10-nm resolution). The **A**s of fine-mode dominated aerosols (i.e., sulfate and smoke) showed higher sensitivity of the n_f and k_f than n_c and k_c (see panels a, b, d, and e in Figure 7), whereas **A** of dust aerosol has comparable or better sensitivity for each mode due to the larger amount of extinction by coarse mode (see panels c and f in Figure 7). The SMART-s measurements can provide not only higher spectral features of n and k but also lower absolute values of $R_{\mathbf{A}}$ (compare panels a with d, b with e, and c with f in Figure 7). The retrieval sensitivity of surface albedo using AERONET-like measurements is still low at $\theta_s = 75°$ and is even lower for the SMART-s measurements.

3.2. Retrieval Error

The OEM provides theoretical/statistical estimate of information content and retrieval error, which can be useful for various applications of the inversion products (Jeong et al., 2016; Rodgers, 1990, 2000). The OEM classifies error sources into four categories. The smoothing error (ε_s, or null space error) is typically generated from insufficient information content or interference between state vectors that have correlated measurement sensitivity. The covariance matrix of ε_s ($\mathbf{S}_s$) is calculated from the bias of **A** from an ideal matrix (i.e., identity matrix, $\mathbf{I}_n$), combined with covariance of the ensemble of states about the mean state ($\mathbf{S}_E$) from following formula:

$$\mathbf{S}_s = (\mathbf{A} - \mathbf{I}_n)\mathbf{S}_E(\mathbf{A} - \mathbf{I}_n)^T. \tag{6}$$

We consider that $\mathbf{S}_a$ well represents this $\mathbf{S}_E$ and have used it for $\mathbf{S}_E$ in this study.

The measurement error consists of random and systematic components that have different impact on the retrieval (e.g., Dubovik et al., 2000). The uncertainties in calibration coefficients are often systematic and included in forward model parameter error (e.g., Rodgers, 1990), whereas measurement precision is random and used for calculation of the retrieval noise (ε_m). Estimation of the ε_m is typically straightforward when an instrument is well monitored, so that reliable error covariance matrix of measurement ($\mathbf{S}_\varepsilon$) is available. The covariance matrix of the ε_m ($\mathbf{S}_m$) can be obtained by

$$\mathbf{S}_m = \mathbf{G}_y \mathbf{S}_\varepsilon \mathbf{G}_y^T. \tag{7}$$

After the absolute radiometric calibration in laboratory and correction of known systematic biases (e.g., temperature sensitivity), we assume remained measurement error is random with absolute value of the AERONET's uncertainty (5%; Holben et al., 1998). Therefore, both random and systematic components of the measurement uncertainties are calculated by the $\mathbf{S}_m$ in this study. Despite retrieval errors from

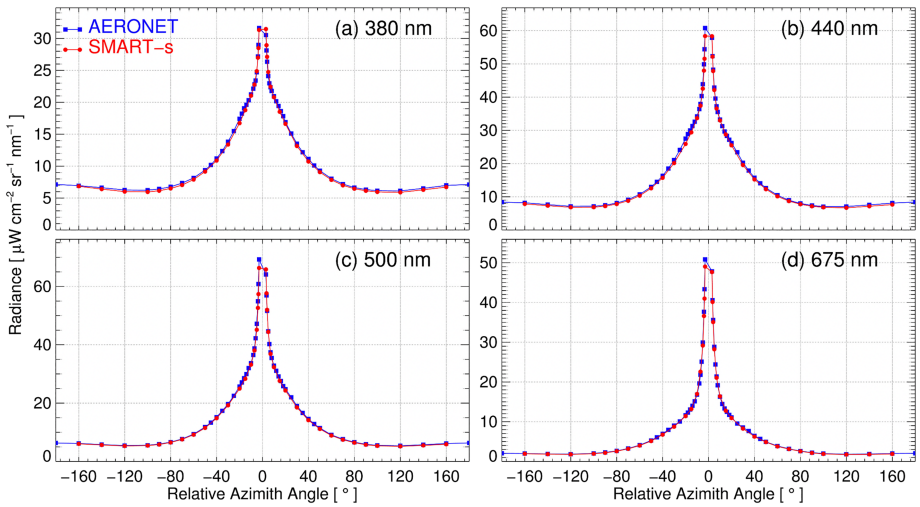

Figure 8. Solar almucantar measurements of SMART-s (red) and AERONET (blue) at (a) 380-, (b) 440-, (c) 500-, and (d) 675-nm wavelengths on 11 December 2017 from the rooftop at NASA/GSFC Building 33. The radiances of SMART-s are arbitrarily scaled to AERONET measurement at ϕ_r of $\pm 3°$ for qualitative comparison.

measurement uncertainty, also considered to be random by this assumption, these values can represent absolute amounts of realistic estimates. Reliable measurement characterization and calibration in a following study will provide more realistic retrieval error from measurement error. Figure 8 shows an example of the almucantar measurements (SZA = 63°) at overlapping wavelengths between SMART-s and AERONET for the symmetry check about the zenith, acquired on 11 December 2017 from the rooftop at NASA/GSFC Building 33. Note radiances of the SMART-s in Figure 8 are arbitrarily scaled to the AERONET measurements at ϕ_r of $\pm 3°$ for qualitative comparison at this moment. This result shows that radiometric linearity of the SMART-s is highly consistent with the AERONET; thus, it can provide comparable accuracy of sky-scan measurements when the instrument is well calibrated.

The forward model error (ε_r) reflects biases between forward model (i.e., RT model in this study) and real atmospheric radiances. The Discrete Ordinate Radiative Transfer-based (Stamnes et al., 1988) models have been widely used for terrestrial remote sensing and intensively compared with measurements as well as other RT models (e.g., Halthore et al., 2005; Jin et al., 2005; van Weele et al., 2000). However, RT calculations using these one-dimensional models can be biased from actual radiances by horizontal heterogeneity of the atmosphere. The pseudo-spherical correction for the Earth's curvature, atmospheric refraction, and surface reflectance estimation also may have nonnegligible uncertainties at extremely high θ_s. We also check symmetry of the sky radiances in the solar almucantar measurements to screen significant horizonal heterogeneity of the atmosphere following Dubovik et al. (2000) and limit the range of θ_s to be less than 75° to avoid these issues. An improved and well-validated forward model may extend these retrieval limits in the future. However, it is challenging to quantify the ε_r, since it typically occurs from lack of understanding of phenomena and/or input data that are hard to obtain (e.g., three-dimensional distributions of atmospheric molecules and particles). Thus, we did not take account the ε_r in this study but minimized its impact.

The model parameters are assumed/fixed parameters that might be part of the state vector but are not being retrieved from the measurements (Rodgers, 1990). The forward model parameter error (ε_f) is generated by these parameters for the inversion, which may be random or systematic. For example, due to the lack of information content of satellite-based measurements, Jeong et al. (2016) presumed aerosol particle size distribution, n, and vertical profile based on climatology and information from other sensors. However, abundant angular information from AERONET and/or SMART-s enables their retrieval algorithm to include most of the major aerosol-related parameters for the state vector (i.e., PSD, n, k, ALH, and ρ). Despite the SMART-s algorithm still constraining some of aerosol-related parameters for the forward model (e.g., PSD is bimodal lognormal distribution, and vertical profile is Gaussian distribution), we consider it can reflect major variabilities of the natural aerosols. Therefore, we assume the ε_r and ε_f from these constraints are

negligible. Based on these assumptions, we defined retrieval error (ε_{ret}) as square root of the sum of squared ε_s and ε_m, which represents the minimum uncertainty of the SMART-s aerosol algorithm.

It is important to understand the significances of each error source to efficiently and effectively improve the retrieval accuracy. For example, when a set of measurements and inversion algorithm are not sufficiently informative, calibration of the measurements may have limited capability for improving the retrievals, and the other way around (e.g., Dubovik et al., 2000). In the Appendix A, we analyzed effects of measurement accuracy and spectral information, which are adjustable and understandable using existing resources, on the retrieval accuracy to understand their significances. In the Appendix B, we described the information contents based on the OE method.

4. Algorithm Consistency Check Using AERONET Measurements

To check consistency of the SMART-s aerosol properties inversion, we applied the algorithm to AERONET's Sun/sky measurements (including near-/shortwave-infrared channels) at Kanpur, India, in 2016. The characteristics of this data set revealed a large amount of fine and coarse mode aerosols persisted throughout the year with τ_{aer} at 500 nm ~0.64 ± 0.33 (mean value ± standard deviation) and Ångström exponent (or AE, between 440 and 870 nm) ~0.98 ± 0.40. Figure 9 shows an example of fitting results of simulated Sun/sky radiances to the measurements on 2 January 2016. Panels from (a) to (g) is for solar almucantar sky radiances from 380 to 1,640 nm, and panel (h) is for spectral τ_{aer}. In this example, the simulated Sun/sky radiances successfully converged to the AERONET measurements after about the fourth step of 10 iterations. We limited fitting residual less than 2% for analysis in this study, which provided 175 retrievals during the period. For the SMART-s high-spectral measurements, we utilize two-step retrieval for numerical efficiency and stability. First, we use measurements with coarse resolution (e.g., with a spectral resolution of 100 nm from 330 to 800 nm). When this step of inversion is successful, these retrievals are used as first guess values and a priori data to execute higher spectral resolution inversion as the next step.

Aerosol PSD is also one of the key parameters for understanding their physio-chemical processes in the atmosphere (e.g., Mahowald et al., 2014; Zhang et al., 2001). Chemical transport models typically utilize multimodal lognormal distributions (e.g., Fairlie et al., 2007; Mahowald et al., 2006) or its modified version (e.g., Kok, 2011; Zhang et al., 2013) to simulate size distribution of the aerosols. We assume a bimodal, lognormal distribution for the aerosols that can be conveniently utilized by such community. Figure 10 compares the retrieved volume size distribution from SMART-s algorithm with the AERONET Version 3, Level 2.0 inversion product (Sinyuk et al., 2020). The lines are annual mean values, and error bars are standard deviation during the period. Black color represents the AERONET operational product, blue color indicates retrieved values, and red color shows their absolute values of difference. The SMART-s aerosol algorithm utilizes stricter constraints of PSD (i.e., bimodal and lognormal number size distribution), whereas the AERONET uses more flexible constraints (i.e., smoothness constraints; see Dubovik & King, 2000). Considering the differences in physical assumptions and numerical methods, they are reasonably consistent, particularly for fine mode (see Figure 10a). However, the coarse-mode PSD retrievals from the SMART-s and AERONET showed relatively higher differences, particularly at the longer tails of SMART-s PSD (ranging from about 10 to 100 μm). It can be attributed to the difference in AERONET's assumption for the PSD. Larger particles are effectively deposited by dry processes; thus, the long tails of coarse mode in Figure 10a may not appear under certain conditions. For example, Ryder et al. (2013) detected dust aerosols with radius up to about 50 μm near source areas. However, about 60% to 90% of the particles with radius greater than 15 μm disappeared after about 12 hr of transport (Ryder et al., 2013). Such deposition processes of large particles may result in uncertainties in coarse-mode PSD retrievals of the SMART-s algorithm, which can affect simulations of radiative impact of aerosols, as well as their interactions with clouds (Mahowald et al., 2014). Panel 10b shows extinction cross section multiplied by the retrieved number size distribution (i.e., the total extinction by particles at each radius node) at the AERONET wavelengths. Note that these values are divided by the maximum value of each channel (normalized). Radiances at shorter wavelengths are more scattered and absorbed by smaller particles, thus have higher retrieval sensitivity for these particles (see plots for shorter wavelength in Figure 10b). Alternately, longer wavelengths are more sensitive to the larger particles. However, there is very small amount of extinction by large particles

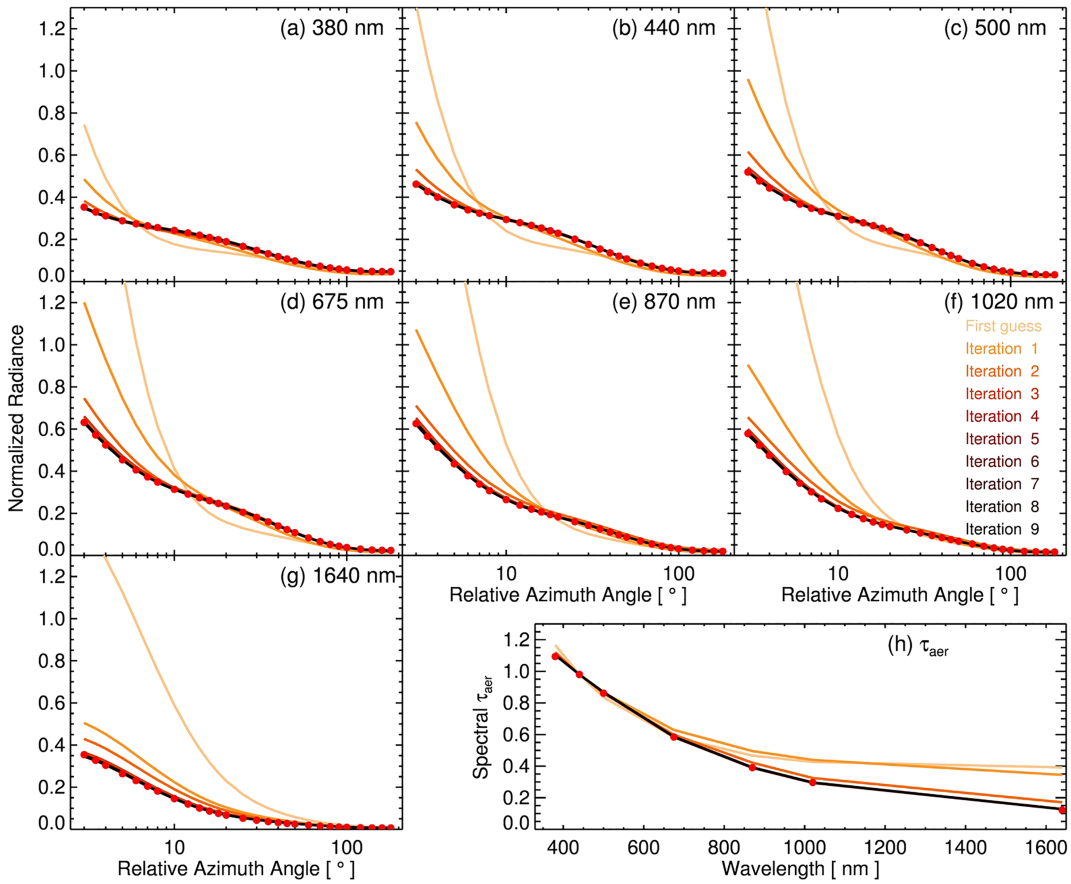

Figure 9. Fitting example of the SMART-s aerosol algorithm to measured Sun/sky radiances of the AERONET at Kanpur, India, at 04:54 UTC on 2 January 2016. (a–g) Solar almucantar sky radiances from 380 to 1,640 nm and (h) spectral τ_{aer}. Solid lines with brighter orange color represent simulated radiances of lower iteration steps and darker colors indicate those of higher-order iterations. The red circles are measured sky radiances (a–g) and τ_{aer} (h) from the AERONET.

(radius greater than about 10 μm) even at longest wavelength (i.e., 1,640 nm; red line in Figure 10b), which results in less retrieval sensitivity of coarse mode PSD. For these reasons, the AERONET algorithm assumes there are no particle radii greater than 15 μm, whereas the SMART-s assumes lognormal distribution for this range and coarse-mode PSD retrievals have higher uncertainties as compared in Appendix A. Note that the bimodal assumption for PSD for the SMART-s algorithm at this stage is for numerical stability and efficiency, but it may also miss important third-mode aerosols (e.g., Eck et al., 2018, 2010; Linak et al., 2002; Ning et al., 1996). By utilizing informative spectral measurements of the SMART-s, we will test for additional parameters for size distribution (e.g., Kok, 2011) or additional modes (trimodes or quadmodes) in a future study to derive optimal information on aerosol size.

Figure 11 compares volume size distribution from the SMART-s algorithm and AERONET product at the AERONET's size bins. Color of the circle represent the 22 radius bins of AERONET retrieval. The root-mean-square error (RMSE), correlation coefficient (r), and mean bias error (MBE) with gray color are calculated using all size bins, whereas black values used small size bins (radius less than 3 μm). In general, retrieved volume size distributions showed good agreements (r = 0.89, RMSE = 0.36, and MBE = 0.07) except for the large bins, due to the differences in their assumptions as discussed. Particularly, the fine-mode PSD retrievals (radius less than 3 μm) are in excellent agreement with the AERONET products during the period (r = 0.98, RMSE = 0.17, and MBE = −0.04).

The spectral ω_0 retrievals from the SMART-s algorithm are compared with the standard AERONET products in Figure 12. Overall, they showed acceptable consistency at all wavelengths with correlation coefficients between 0.87–0.95 and absolute mean bias errors less than 0.01. The ω_0 retrievals at 1,020 nm from both

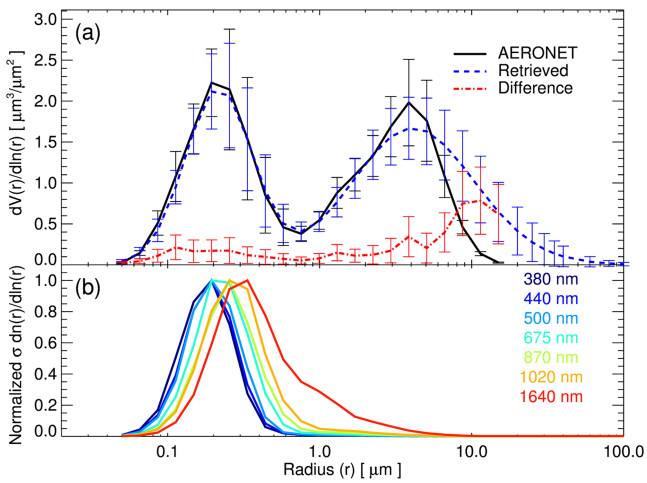

Figure 10. (a) Comparison of successful retrievals (175 samples with fitting residuals less than 2%) of aerosol volume size distribution from the SMART-s using AERONET's Sun/sky measurements (blue) and AERONET (black) products at Kanpur, India, in 2016. The red color indicates mean value of absolute differences between retrievals from the SMART-s and AERONET algorithm, and the error bar is standard deviation of the differences. (b) Extinction cross section multiplied by the retrieved number size distribution (i.e., total extinction by particles at each radius node) at the AERONET wavelengths. The lines in panel (b) then divided by maximum values of each channel (normalized). Panel (b) indicates that the longer tails of SMART-s PSD retrievals ranging from about 10 to 100 μm, which shows large differences from the AERONET product, have negligible sensitivity to the measurements.

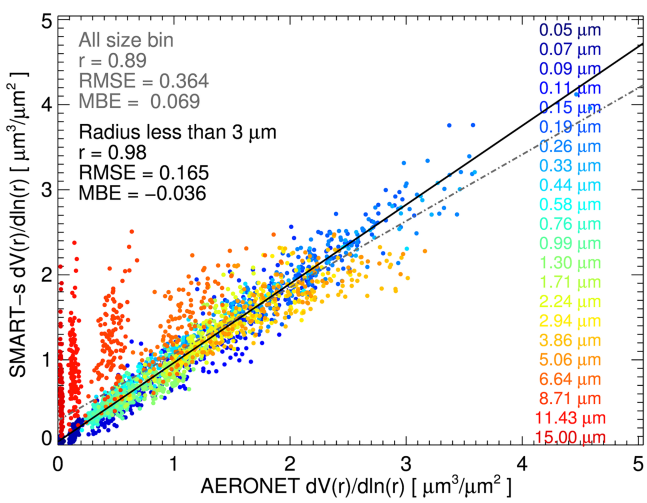

Figure 11. Comparison of volume size distribution from the SMART-s algorithm using AERONET's Sun/sky measurements and AERONET product at Kanpur, India, in 2016. Color of the circle represent 22 radius bins of AERONET retrieval. RMSE denotes root-mean-square error, r is the correlation coefficient, and MBE is the mean bias error. The statistics with gray color is calculated using all size bins, whereas the black values used small size bins (radius less than 3 μm). The grey dot-dashed line and black solid line represent regression slopes for all size bin and small size bin (radius less than 3 μm), respectively.

algorithms were more scattered compared to other wavelengths due to lower τ_{aer} at 1,020 nm during fine mode dominated period (see Figure 12d). Additional importance of the aerosol absorption is that it is one of the key parameters for calculating the air mass factor for both satellite- and ground-based trace gas retrievals (e.g., Hong et al., 2017). The highly resolved spectral ω_0 from SMART-s, covering whole spectral range of the instrument, directly provides the retrieved value without assumption of aerosol properties or interpolation. Therefore, trace gas profile inversions using this information can further improve their accuracy, which will be followed in the next step of SMART-s inversion package (see Figure 2).

Panels a and b in Figure 13 shows temporal variations in the n and k from the SMART-s (red squares for fine mode and blue diamonds for coarse mode) and AERONET (black circles) at 675 nm at Kanpur, India, in 2016. Panel c is the Ångström exponent (AE) between 440 and 870 nm during the same period. Larger symbols with error bar represent the monthly mean and standard deviation and smaller (and faint) symbols are successful retrievals with fitting residuals less than 2%. Note that the statistical sampling of the SMART-s is different from the AERONET due to their different fitting residuals. Fine and absorbing aerosols confined within the shallow planetary boundary layer during the winter monsoon climate in the Indo-Gangetic plain results in larger values of AE with low standard deviation (panel c) and relatively high values of k_f (panel b) as shown in Figure 13 (Eck et al., 1999). As the summer monsoonal flow strengthened, coarse-mode dust aerosols either from local (e.g., Thar desert) or distant sources (e.g., deserts in Arabian Peninsula) mixed with other type of aerosols (e.g., biomass burning and other anthropogenic aerosols) dominates this area from April to July (e.g., Giles et al., 2011). The heterogeneity of aerosol leads to smaller values of AE with larger variabilities during this period as shown in panel c. The SMART-s retrievals did not converge within acceptable agreement (i.e., 2%) during this period, which may be attributed to nonspherical shape of the dust particles (Implementation of T-matrix code to account for nonspherical aerosols are underway; Mishchenko et al., 2010; Spurr et al., 2012; Yang et al., 2007). However, the SMART-s algorithm provided reliable retrievals of the n and k during winter time when fine-mode aerosols prevail.

The n_f from the SMART-s is slightly lower than n from AERONET but has similar temporal variations as shown in Figure 13a, since measurement sensitivity of n is dominated by fine-mode particles during the period. Therefore, this partially shows consistency of the n retrievals from SMART-s with the AERONET algorithm. The n_c retrievals of SMART-s were relatively higher and more scattered as shown in panel a. As compared in Appendix A (*compare* the black circles in between panels a and b in Figure A2), estimated ε_{ret}s of n_c (~0.075) is more than 2 times higher than n_f (~0.03) at 675 nm, which may affect the large variability and hitting lower boundary (n = 1.33) of the n_c in Figure 13a. The k_f from the SMART-s also showed similar temporal variations with k from AERONET, whereas that of k_c was different as shown in Figure 13b. The k_c (675 nm) retrievals of SMART-s were relatively higher than AERONET with a slightly larger variability even with their comparable estimated retrieval accuracy than fine mode as compared in Appendix A (*compare* the black circles in between panels c and d in Figure A2).

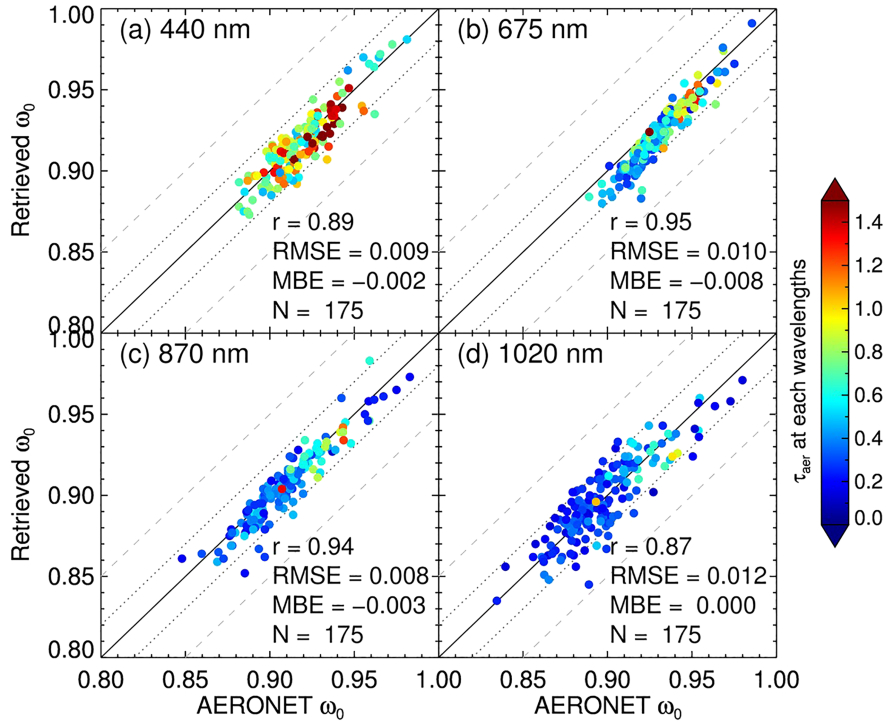

Figure 12. Comparison of successful retrievals (175 samples with fitting residuals less than 2%) of single-scattering albedo from the SMART-s algorithm using AERONET's Sun/sky measurements and AERONET product at (a) 440, (b) 675, (c) 870, and (d) 1,020 nm. The measurement data are at Kanpur, India, in 2016. Color of the circle represents aerosol optical thickness at each wavelength. RMSE denotes root-mean-square error, *r* is the correlation coefficient, MBE is the mean bias error, and N is the number of samples for the comparison. The dotted line and dashed line represent relative biases of ±0.02 and ± 0.05 from the AERONET product.

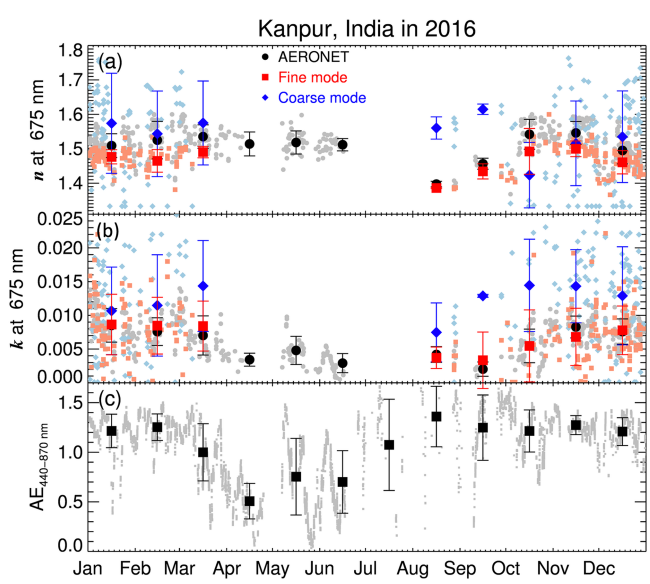

Figure 13. Time series of (a) real part and (b) imaginary part of refractive index retrievals from the AERONET and SMART-s algorithm using AERONET's Sun/sky measurements at Kanpur, India, in 2016. (c) Ångström exponent between 440 and 870 nm during the same period. Dark symbols with error bars represent monthly means and standard deviations, and smaller, brighter symbols are all retrievals with fitting residuals less than 2%.

Therefore, the significant variabilities of the n_c and k_c in Figure 13 also can be attributed to diversity of dust composition and their microphysical properties (e.g., Gillespie & Lindberg, 1992; Sokolik & Toon, 1999; Zhang et al., 2017). In general, the retrievals of *n* and *k* are estimated to be highly uncertain, particularly for coarse mode (e.g., Sinyuk et al., 2020), which result in noisy values in Figures 13a and 13b. Therefore, it can mislead users when reliable error estimates are absent. Accurate error estimates of these retrievals from the OE method can help users to reliably assess/understand the retrievals and utilize them properly (e.g., using averaged value of the n_c and k_c over a long period). Therefore, we expect retrievals of the *n* and *k* for each size bin with realistic error estimates can provide valuable information on aerosol chemistry, thereby, their impacts on the Earth's terrestrial system. We also checked the consistency of the SMART-s algorithm with AERONET at Seoul, South Korea, where more scattering fine-mode aerosols prevail, in Appendix C.

Recent advanced instruments, for in situ and/or laboratory environments, enable precision measurements of spectral ($n + ik$) of various aerosol species. For example, Washenfelder et al. (2013) measured high resolution of complex refractive indices (spectral range 360–420 nm) for aerosol types varying from purely scattering (e.g., ammonium sulfate), slightly absorbing, to strongly absorbing (e.g., nigrosin dye). Similarly, Flores, Washenfelder et al. (2014), Flores, Zhao et al. (2014) measured *n* and *k* of secondary organic carbons and reported their spectral/temporal

variations as they aged. Moreover, based on the Cauchy equation, Shepherd et al. (2018) retrieved the n and k of insoluble organic extracts by applying a new technique of optical trapping combined with Mie spectroscopy and revealed significant spectral variation from 460 to 700 nm depending on aerosol composition. As variabilities of the reported n are typically comparable or larger than the estimated ε_{ret} of n, combination of the SMART-s retrievals with these laboratory and in situ measurements can enable reliable aerosol type partitioning based on spectral analysis technique (e.g., Hansell et al., 2014). The combination of aerosol chemical information with trace gas retrievals from sufficient measurements can contribute reliable source apportionment of the air pollutants (e.g., Jeong et al., 2017; Schauer & Cass, 2000). Furthermore, accurate chemical and size information of aerosols are also critical to estimate hygroscopicity of different types of aerosols and their impact on cloud formation (e.g., Chang et al., 2017; Dusek et al., 2006; Eck et al., 2018; Facchini et al., 2000; Hao et al., 2013; Mochida et al., 2011; Schmale et al., 2018; Väisänen et al., 2016, and references therein). Therefore, simultaneous retrievals of trace gases (e.g., NO_2, SO_2, H_2O, and O_3) and aerosol properties by SMART-s can provide unique opportunities to monitor the evolution processes of atmospheric trace gases and aerosols including emission, gas-to-particle conversion, and information on cloud formation.

5. Summary

In this study, we present the first part of the theoretical basis of SMART-s trace gas and aerosol inversion package, utilizing an OEM to retrieve column properties of atmospheric aerosols from the direct Sun/sky spectral measurements. Data products include column abundance of trace gases, aerosol spectral optical thickness, and single-scattering albedo, as well as particle size distribution and spectral $(n + ik)$ of fine- and coarse-mode aerosols. One of the key advantages of the SMART-s aerosol inversion products is high spectral-resolution refractive indices from near-UV to near-IR wavelengths for each size mode, which is crucial information for atmospheric chemistry and climate studies, as well as for retrieving vertical profiles of aerosols and trace gases in the second part of the SMART-s algorithm.

The OE-based SMART-s algorithm provides reliable error estimates, which is particularly useful for relevant studies using higher-order retrievals with larger uncertainties (e.g., aerosol spectral $[n + ik]$). Theoretically, the estimated information content of the SMART-s algorithm indicates that it can provide independent information on spectral $(n + ik)$ of fine- and coarse-mode aerosols. In Appendix A, we also compared different types of synthetic measurements (e.g., AERONET-like, Pandora, and SMART-s) used in the algorithm. Estimated retrieval errors of PSD and refractive indices retrievals using the SMART-s measurements are lower than those using other types of measurements with a same level of radiometric accuracy. Both accurate radiometric calibration of sky-radiances and high spectral resolution of measurements are important for most of the aerosol parameters (see Appendix A). Furthermore, to assess its consistency with the well-validated AERONET algorithm, the SMART-s retrieval algorithm was applied to a yearlong set of AERONET Sun/sky measurements at Kanpur, India, in 2016. Despite the use of different forward RT models and inversion methods, the retrieved aerosol parameters from the SMART-s algorithm revealed reasonable agreement with the AERONET operational (i.e., Version 3, Level 2.0) products (e.g., for spectral ω_0 retrievals, correlation coefficients between these two products were 0.87–0.95, and absolute mean bias errors were less than 0.01).

Appendix A: Effects of Measurement Accuracy, Spectral Resolution, and Aerosol Type on Retrieval Error

Figure A1 shows estimated retrieval errors (ε_{ret}) of the particle-size distribution (PSD) parameters as a function of radiometric calibration accuracy (from 1% to 7%) of the solar almucantar measurements. Here 1% represents an ideal case of radiometric calibration and stability of the SMART-s, which is comparable to the NIST-traceable lamp. The 7% is a conservative value, 2% higher than uncertainty of the AERONET sky-scan measurements reported by Holben et al. (1998). The symbols and error bar represent the mean and standard deviation of ε_{ret} calculations for various conditions (θ_s of 50° — 75° at 5° interval, for the three aerosol types). The black line with diamond symbol represents the AERONET-like measurements, the blue line with squares is for the standard Pandora measurements (330 to 530 nm with a 10-nm resolution), and the red line with circles reflects SMART-s measurements (330 to 800 nm with a 10-nm resolution). The

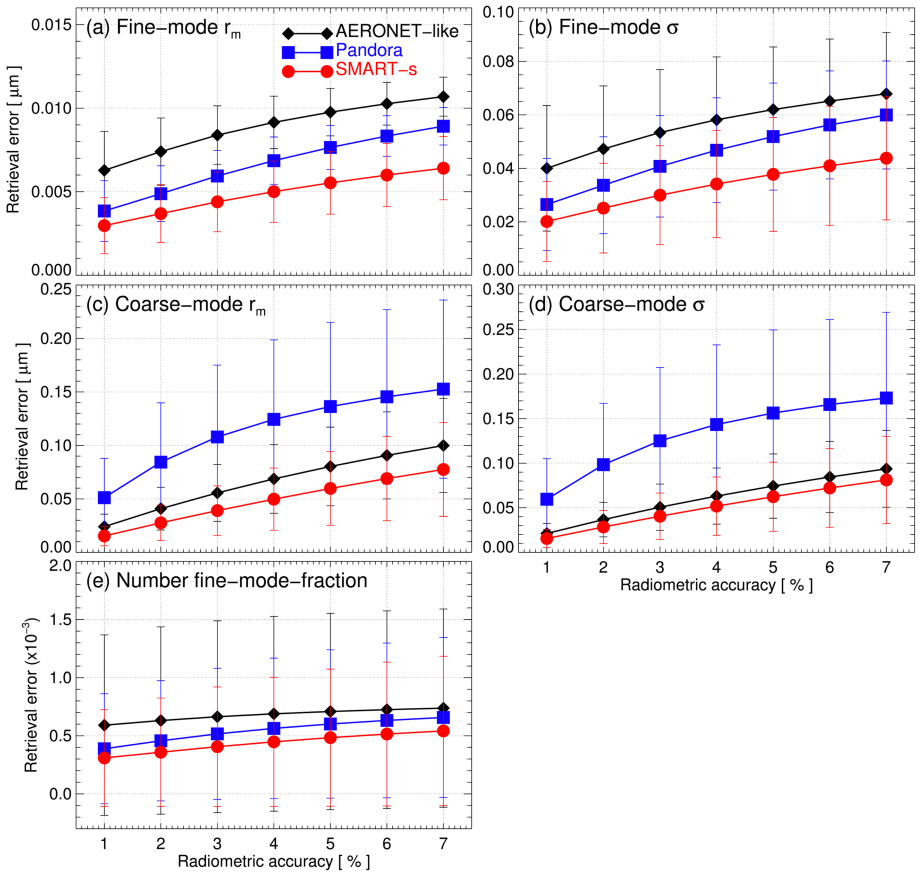

Figure A1. Estimated ε_{ret}s of the (a) r_f, (b) σ_f, (c) r_c, (d) σ_c, and (e) F_{num} as a function of radiometric calibration accuracy of the solar-almucantar measurements. The symbols and error bar represent mean and standard deviation of the calculations for various conditions (θ_s of 50°–75° at 5° interval, for the three aerosol types). The black line with diamond symbol represents AERONET-like measurements, the blue line with squares is for the standard Pandora measurements (330 to 530 nm with a 10 nm resolution), and the red line with circles reflects SMART-s measurements (330 to 800 nm with a 10-nm resolution).

ε_{ret}s of PSD parameters using the SMART-s measurements are estimated to be lower than other types of measurements. The Pandora measurements are expected to provide more reliable information on fine-mode PSD parameters than those of AERONET-like measurements (see Figures A1a and A1b), due to finer spectral information in the shorter visible bands which are more sensitive to fine mode aerosols (see Figure 10b). However, the AERONET-like measurements are more sensitive for r_c and σ_c than Pandora due to the additional spectral information from the longer infrared wavelengths, which are more sensitive to coarser aerosols (Figures A1c and A1d). The lower spectral resolution of AERONET-like measurements is complimented by their broader spectral coverage (i.e., up to 1,640 nm) so that its estimated ε_{ret} of r_c and σ_c are comparable to those using the SMART-s. The differences in ε_{ret} of number fine-mode fraction (F_{num}) for the three types of measurements are insignificant regarding their variability on different θ_s conditions and aerosol types (see Figure A1e). Accuracy of radiometric calibration has the most significant impact on coarse mode PSD. When the radiometric accuracy improved from 7% to 1%, the ε_{ret} of r_c and σ_c reduced by about 70% (Figures A1c and A1d). This level of radiometric improvement is also important on fine mode PSD retrievals, which reduced ε_{ret} of r_f and σ_f by about 45% (Figures A1a and A1b). The radiometric performance of the instruments has less effect on F_{num} retrievals as shown in Figure A1e.

The measurement accuracy is also important for retrievals of the complex index of refraction. Figure A2 shows ε_{ret}s of the spectral n and k for different radiometric accuracy from 1% to 7%. The lines with blue color series represent the Pandora, and those with red color series are for the SMART-s. The spectral resolution of

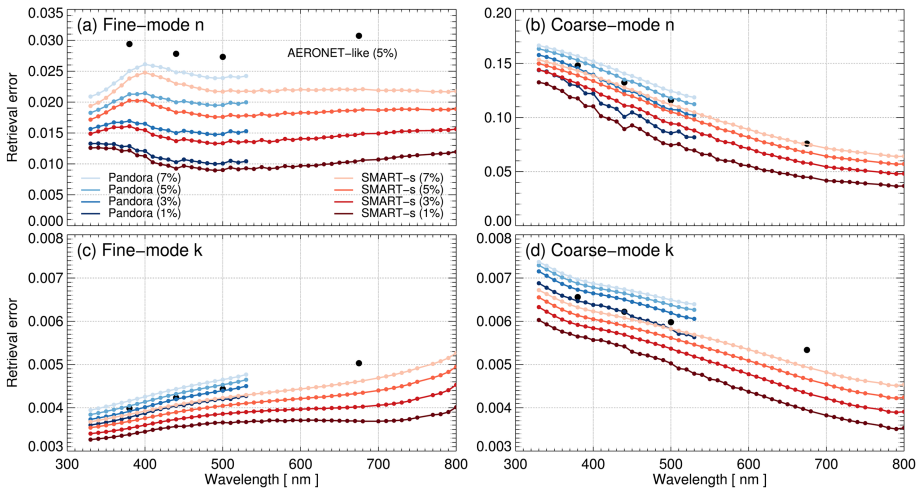

Figure A2. Estimated retrieval errors of the real-part-refractive index (n) of (a) fine- and (b) coarse-mode aerosols using the AERONET-like (black circles), the Pandora (blue color series lines), and the SMART-s (red color series lines) measurements with different levels of radiometric accuracy from 1% to 7%. Panels (c) and (d) are similar plots but for imaginary-part-refractive index (k) of fine- and coarse-mode aerosols, respectively.

the SMART-s and the Pandora for this analysis is also 10 nm. The black circles are estimated $\varepsilon_{\mathrm{ret}}$s of the spectral n and k using AERONET-like measurements with 5% of radiometric accuracy. In general, high-spectral resolution of measurements from the SMART-s and the Pandora is expected to provide comparable or better information on spectral n_{f} and n_{c} than those from AERONET-like measurements, within their spectral coverage. We also expect the n_{f} retrievals are about an order of magnitude more accurate than the n_{c} retrievals using the all types of measurements, which can be attributed to more dynamic variation of the phase function of fine mode aerosols in the visible wavelengths (compare Figures A2a and A2b). The radiometric accuracy is important for n, particularly for n_{f}, as shown in Figures A2a and A2b. When same levels of measurement accuracies are given, estimated $\varepsilon_{\mathrm{ret}}$s of n_{f} and n_{c} using the SMART-s are lower than that using Pandora with SMART-s broader spectral coverage (see Figures A2a and A2b). We also estimate better retrievals of k_{f} than k_{c}, with their opposite spectral features (see Figures A2c and A2d). The lower $\varepsilon_{\mathrm{ret}}$s of k_{f} retrievals in shorter wavelengths are due to more efficient extinction by fine mode particles and vice versa for k_{c}. The k_{f} has critical importance for monitoring the role of carbonaceous aerosols in tropospheric photochemistry and air quality (e.g., Castro et al., 2001; Dickerson et al., 1997; He & Carmichael, 1999). Particularly, absorbing components of organic aerosols (or sometimes called as brown carbon) have significant light absorption efficiency in the UV with strong wavelength dependence, which result in high UV absorption compared to visible or infrared wavelengths in various field and laboratory measurements (e.g., Chen & Bond, 2010; Kirchstetter et al., 2004; Martins et al., 2009; Mok et al., 2016, 2018; Saleh et al., 2013; Zhong & Jang, 2014). Mok et al. (2016) retrieved spectral ω_0 from UV to near infrared using combined data set from AERONET, MFRSR, and Pandora and quantified effects of the brown carbon on ozone photochemistry in the Amazon Basin. We expect the spectral ω_0 retrievals covering UV wavelengths from the SMART-s (and possibly from the AERONET and Pandora networks) will provide global information on these carbonaceous aerosols, as well as other types. Radiometric accuracy also has meaningful impact on the k_{f} and k_{c} retrievals as shown in Figures A2c and A2d.

As described in section 2, the SMART-s does not require a longer time between measurements for higher spectral resolution, since it measures all wavelengths at a same time. Thus, its retrieval algorithm can adjust the wavelengths for the inversion up to about the spectrometer's spectral range and maximum resolution. In general, more information is available from higher spectral resolution for a given spectral range. However, larger dimensions of $\mathbf{y}$ and $\mathbf{F}$ also require increased numerical cost and, more importantly, can cause higher risk of instability and of finding an incorrect local minimum instead of the absolute minimum from the

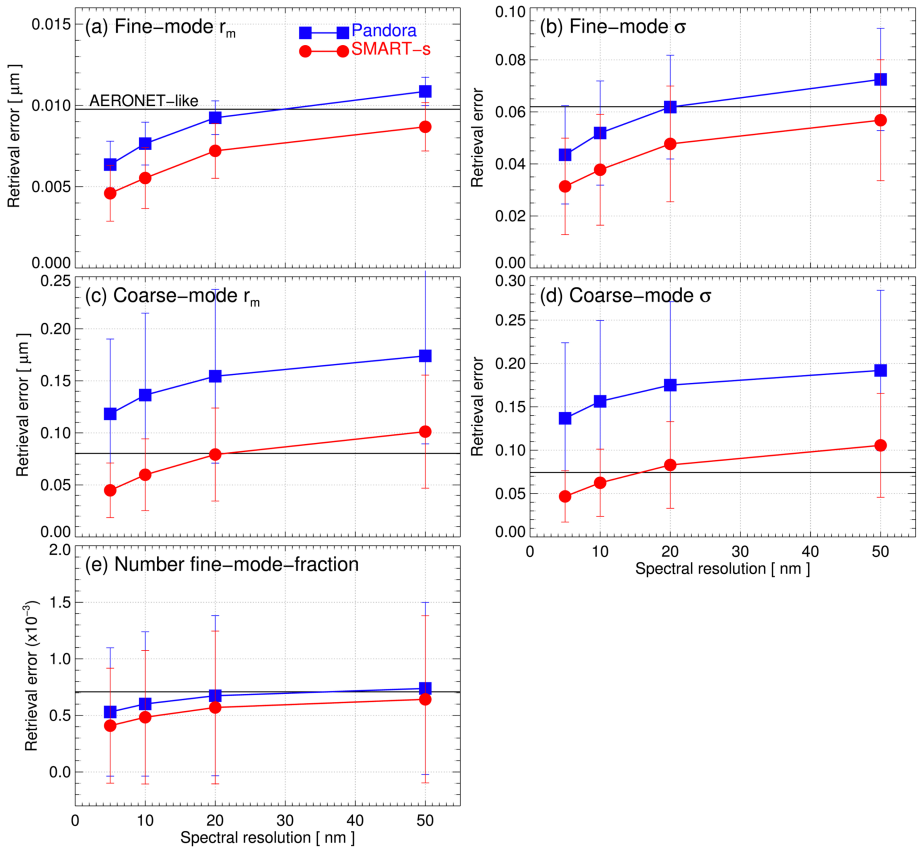

Figure A3. Estimated $\varepsilon_{\mathrm{ret}}$s of the (a) r_{f}, (b) σ_{f}, (c) r_{c}, (d) σ_{c}, and (f) F_{num} as a function of spectral resolution of the SMART-s and the Pandora measurements. The black line represents the AERONET-like measurements at seven fixed wavelengths from 380 to 1640 nm, the blue line with squares is for the spectral coverage of Pandora (330 to 530 nm), and the red line with circles reflects that of SMART-s (330 to 800 nm). The symbols and error bar represent mean and standard deviation of the calculations for various conditions (θ_{s} of 50°–75° at 5° interval, for the three aerosol types).

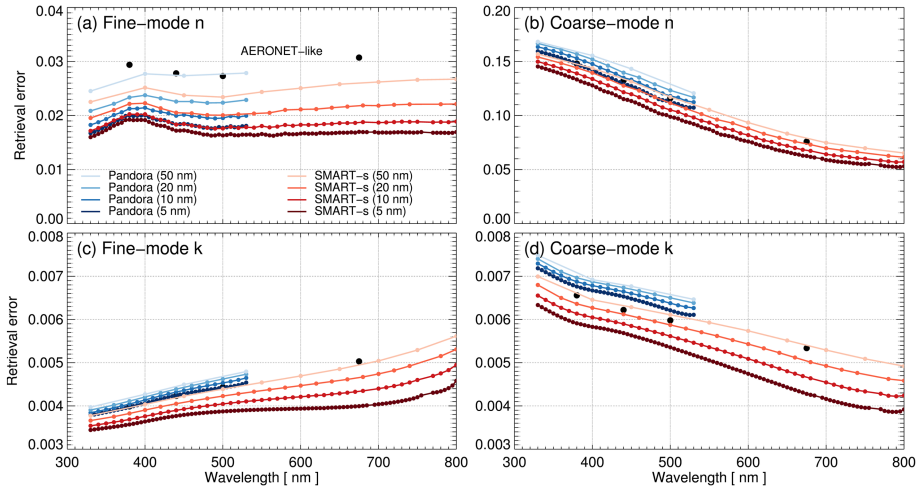

Figure A4. Estimated retrieval errors of real-part-refractive index (n) of (a) fine- and (b) coarse-mode aerosols using the AERONET-like (black circles), the Pandora (blue color series lines), and the SMART-s (red color series lines) measurements with different spectral resolutions from 5 to 50 nm. (c and d) Similar plots but for imaginary-part-refractive index (k) of fine- and coarse-mode aerosols, respectively.

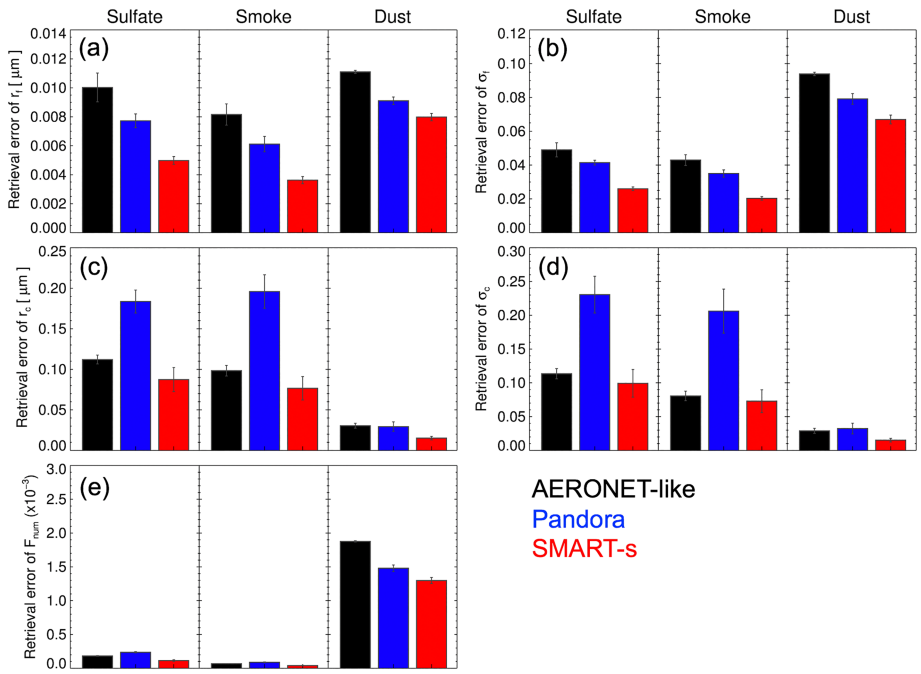

Figure A5. Estimated mean value of ε_{ret}s of the (a) r_f, (b) σ_c, (c) r_c, (d) σ_c, and (f) F_{num} for different type of aerosols and instruments. The black bar represents the AERONET-like measurements, the blue bar is for the Pandora, and the red bar reflects that of SMART-s. The error bar represents standard deviation of the calculations for various θ_ss (50°–75° at 5° interval).

inversion. The spectral features of light extinction by aerosols are typically smoother than trace gas absorptions. Therefore, too high spectral resolution for **y** also can introduce unwanted spectral noise from trace gases with less benefit for aerosols. The total column retrievals of trace gases from the prior step in Figure 2 can reduce their effect on aerosol retrievals. However, even a small error of information on atmospheric gases can generate nonnegligible uncertainties in the aerosol retrieval, particularly near strong absorption bands (e.g., oxygen and water vapor). Therefore, we will determine final wavelengths

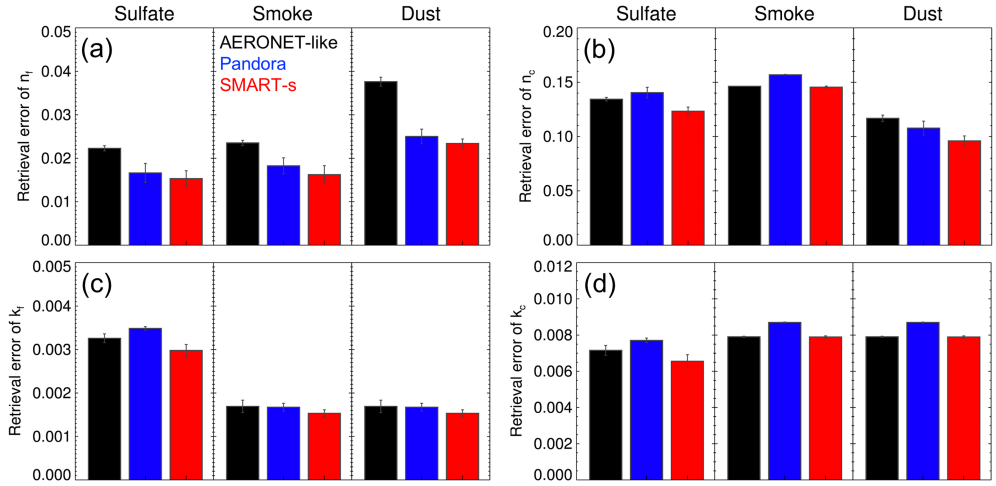

Figure A6. Estimated retrieval errors of real-part-refractive index (n) at 440 nm of (a) fine- and (b) coarse-mode aerosols (for sulfate, smoke, and dust type defined in the manuscript) using the AERONET-like (black bar), the Pandora (blue bar), and the SMART-s (red bar). (c and d) Similar plots but for imaginary-part-refractive index (k) of fine- and coarse-mode aerosols, respectively.

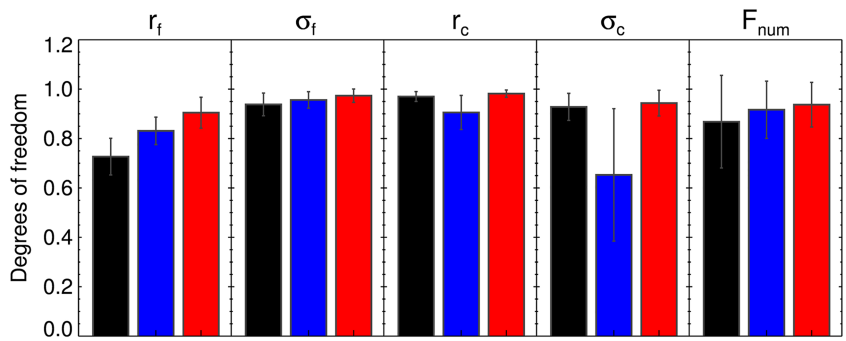

Figure B1. Estimated mean value of degrees of freedom for the particle size distribution parameters (*i.e.*, r_f, σ_c, r_c, σ_c, and F_{num}). The black bar represents the AERONET-like measurements, the blue bar is for the Pandora, and the red bar reflects that of SMART-s. The error bar represents standard deviation of the calculations for various conditions (θ_s of 50°–75° at 5° interval, for the three aerosol types).

for the SMART-s aerosol inversion regarding such aspects for practical implementation based on intensive tests and radiometric calibrations.

Figure A3 shows estimated ε_{ret}s of the PSD parameters as a function of utilized spectral resolutions (5, 10, 20, and 50 nm) of the SMART-s (red circles with line) and the Pandora measurements (blue squares with line). The black flat line in Figure A3 represents those parameters only from the AERONET's full range of spectral measurements (380–1640 nm). The radiometric accuracy of the measurements for this analysis is 5%. The number of wavelengths for these resolutions for the SMART-s is 95, 48, 24, and 10, whereas those for the Pandora are 41, 21, 10, and 4, respectively (the number of wavelengths of the AERONET-like measurements is held constant at seven).

More reliable PSD retrievals are expected by utilizing higher spectral resolution of the SMART-s and Pandora measurements as shown in Figure A3. Estimated ε_{ret}s of the fine-mode PSD parameters using the SMART-s measurements are lower than the AERONET-like measurements even using a 50-nm resolution, whereas the Pandora needs to use a resolution better than 20 nm to provide comparable PSD retrievals using the AERONET-like measurements (see Figures A3a and A3b). For coarse-mode PSD retrievals, we also estimate the SMART-s provides comparable retrieval accuracy to AERONET-like measurements even with

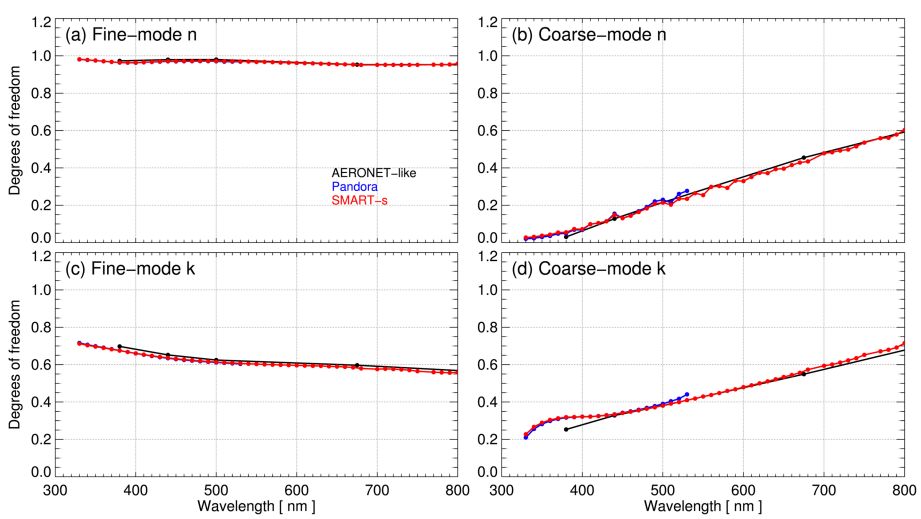

Figure B2. Estimated degrees of freedom for signal of the real-part-refractive index (n) of (a) fine- and (b) coarse-mode aerosols using the AERONET-like (black), the Pandora (blue), and the SMART-s (red) measurements. (c and d) Similar plots but for imaginary-part-refractive index (k) of fine- and coarse-mode aerosols, respectively.

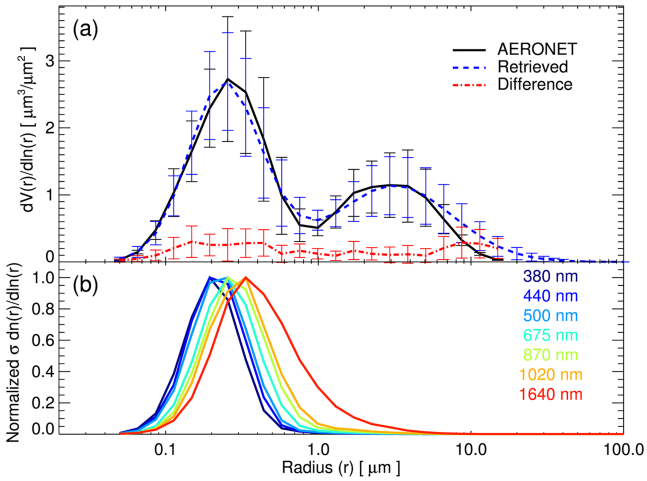

Figure C1. (a) Comparison of successful retrievals (21 samples with fitting residuals less than 2%) of aerosol volume size distribution from the SMART-s using AERONET's Sun/sky measurements (blue) and AERONET (black) products at Seoul, South Korea, in 2016. The red color indicates mean value of absolute differences between retrievals from the SMART-s and AERONET algorithm, and the error bar is one standard deviation of the differences. (b) Extinction cross section multiplied by the retrieved number size distribution (i.e., total extinction by particles at each radius node) at the AERONET wavelengths.

50-nm resolution. However, the ε_{ret}s of r_c and σ_c from 5-nm resolution of Pandora measurements re still higher than those from the AERONET-like measurements (see Figures A3c and A3d). The differences in ε_{ret} of F_{num} for the three types of measurements are small compared to their variability for different θ_s and aerosol types (see the error bars in Figure A3e). The spectral resolution is comparably important for each mode PSD retrievals, whereas it has less effect on F_{num} retrievals.

Figure A4 shows the ε_{ret}s of spectral n and k using different spectral resolutions. The lines with blue color series represent the Pandora, and those with red color series are for the SMART-s (darker color indicates higher spectral resolution, from 50 to 5 nm). The black circles are estimated ε_{ret}s of the spectral n and k using AERONET-like spectral measurements. Radiometric accuracy of these measurements for the analysis is also assumed to be 5%. In general, higher spectral resolution of measurements from the SMART-s and the Pandora is expected to provide comparable or slightly better accuracy on spectral n and k than those from AERONET-like measurements, within their spectral coverage. Measurements with higher spectral resolution have meaningful impacts on the spectral n and k retrievals from the Pandora and SMART-s as shown in Figure A4. When the same spectral resolution is given, estimated ε_{ret}s of n and k for both modes using SMART-s are lower than those using Pandora with SMART-s broader spectral coverage. Interestingly, benefit of using finer spectral resolution for the n and k retrievals is larger for the SMART-s than Pandora, with their more informative spectral features.

Figure A5 compares estimated retrieval errors (ε_{ret}) of the particle size distribution (PSD) parameters for different type of aerosols (i.e., sulfate, smoke, and dust). The error bar represents one standard deviation of ε_{ret} calculations for various θ_ss (50° — 75° at 5° interval). The black bar represents the AERONET-like measurements, the blue bar is for the standard Pandora measurements (330 to 530 nm with a 10-nm resolution), and the red bar reflects SMART-s measurements (330 to 800 nm with a 10-nm resolution). The ε_{ret}s of PSD parameters using different types of measurements are consistent with the results in Figures A1–A4. Estimated retrieval accuracy of the r_f and σ_f for fine-mode aerosols (i.e., sulfate and smoke) is better than those for dust aerosols due to the stronger extinction by fine-mode particles (see Figures A5a and A5b). In the other way around, the r_c and σ_c retrievals of dust particles are estimated to be more accurate than sulfate and smoke aerosols (see Figures A5c and A5d). The estimated ε_{ret}s of F_{num} retrievals for sulfate and smoke aerosols are about an order magnitude lower than that for dust as shown in Figure A5e.

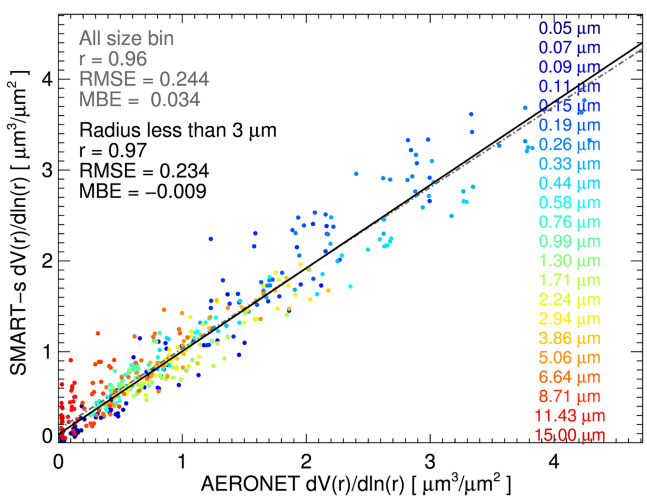

Figure C2. Comparison of volume size distribution from the SMART-s algorithm using AERONET's Sun/sky measurements and AERONET product at Seoul, South Korea, in 2016. Color of the circle represent 22 radius bins of AERONET retrieval. RMSE denotes root-mean-square error, r is the correlation coefficient, and MBE is the mean bias error. The statistics with gray color is calculated using all size bins, whereas the black values used small size bins (radius less than 3 μm). The grey dot-dashed line and black solid line represent regression slopes for all size bin and small size bin (radius less than 3 μm), respectively.

Figure A6 is similar plot with A5 but for the n and k at 440 nm (here 440 nm is the unique channel that operational AERONET products, AERONET-like, Pandora, and SMART-s retrievals overlap). In general, the ε_{ret}s for n and k at 440 nm using different types of measurements are also consistent with the results in Figures A1–A4. Estimated retrieval accuracy of the n_f for fine-mode aerosols (i.e., sulfate and smoke) is better than those for dust aerosols due to the stronger scattering by fine-mode particles, thus more information on their phase function (see Figure A6 a). For the same reason, the n_c retrievals of dust particles are slightly more accurate than sulfate and smoke aerosols (see Figure A6b). The estimated ε_{ret}s of k_f retrievals for sulfate aerosols are higher than those for smoke and dust aerosols, whereas the ε_{ret}s of k_c retrievals are comparable for all type of aerosols (see Figures A6c and A6d).

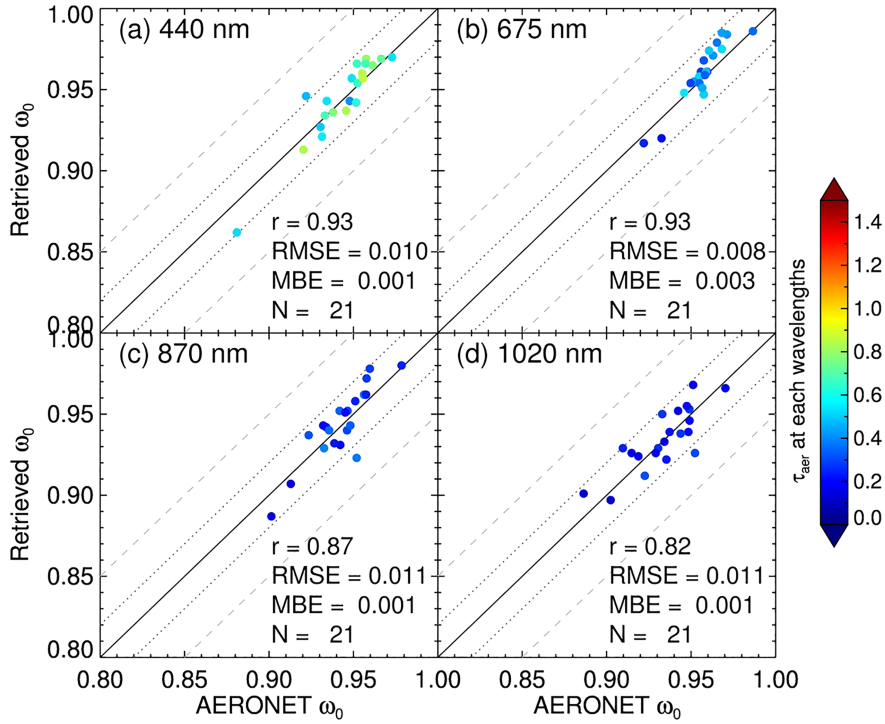

Figure C3. Comparison of successful retrievals (21 samples with fitting residuals less than 2%) of single-scattering albedo from the SMART-s algorithm using AERONET's Sun/sky measurements and AERONET product at (a) 440, (b) 675, (c) 870, and (d) 1,020 nm. The measurement data are from Seoul, South Korea, in 2016. Color of the circle represents aerosol optical thickness at each wavelength. RMSE denotes root-mean-square error, r is the correlation coefficient, MBE is the mean bias error, and N is the number of samples for the comparison. The dotted line and dashed line represent relative biases of ±0.02 and ± 0.05 from the AERONET product.

Appendix B: Degrees of Freedom for Signal

Figure B1 shows the degrees of freedom for the signal (d_s; diagonal elements of the averaging kernel matrix) for PSD parameters using different types of instruments. The error bar represents standard deviation of these values for various conditions (θ_s of 50°–75° at 5° interval, for the three aerosol types). The black bar is for the AERONET-like measurements, the blue bar represents the standard Pandora measurements (330 to 530 nm with a 10-nm resolution), and the red bar reflects SMART-s measurements (330 to 800 nm with a 10-nm resolution). In general, we estimate that all types of instruments can provide informative PSD retrievals (d_s close to one). According to the result, the SMART-s provides comparable or more informative PSD retrievals, particularly for the r_f. The Pandora measurements have least d_s for the coarse-mode PSD parameters, due to their narrower spectral coverage.

Figure B2 shows the d_s of spectral complex refractive indices for fine and coarse modes using different instruments. The black is for the AERONET-like measurements, the blue represents the standard Pandora measurements (330 to 530 nm with a 10-nm resolution), and the red reflects SMART-s measurements (330 to 800 nm with a 10-nm resolution). All types of measurements are very sensitive to the fine mode n at all wavelengths, which results in d_s values close to one (Figure B2a). We also expect informative retrievals of the k_f using the three types of measurements as shown in Figure B2c (d_s ~0.6). However, the d_ss of coarse-mode refractive indices appear to be low with their significant spectral feature as shown in Figures B2b and B2d (higher d_s of n_c and k_c at longer wavelengths). Therefore, the n_c and k_c retrievals can significantly depend on the a priori data (or noisy as in Figure 13), particularly at shorter wavelengths.

Appendix C: Consistency Check of the Algorithm in Seoul, South Korea

Figures C1–C3 are similar plot with Figures 10–12, respectively but for another site at Seoul, South Korea (Yonsei University). This AERONET site also has long-term records with high aerosol loading. However,

due to less amounts of aerosols and sunny days compared to the Kanpur site, it has smaller number of successful retrievals. Seoul is mostly dominated by fine-mode aerosols (see Figure C1) with higher single-scattering albedo compared to Kanpur (Figure C3). However, the PSD and ω_0 retrievals from the SMART-s algorithm also showed reasonable consistency with the AERONET product (Version 3, level 2.0), as compared in Figures C1–C3.

Acknowledgments
This research was under the project of *Understanding Changes in High Mountain Asia*, as part of NASA Cryosphere Program. Authors of Jeong/Tsay gratefully acknowledge the continuous support of NASA Radiation Sciences Program, managed by Hal B. Maring, on the research development of SMART-s, deployments of the SMARTLabs, and the execution of this study. NASA Earth Observing System and RSP provide facility supports of AERONET. We also acknowledge Barry L. Lefer, Program Manager of the NASA Tropospheric Composition Program, and his support of the NASA Pandora Project (https://pandora.gsfc.nasa.gov) located at NASA Goddard Space Flight Center. The SMART-s data are available at https://smartlabs.gsfc.nasa.gov, and the AERONET data are available at https://aeronet.gsfc.nasa.gov website.

References

Ancellet, G., Pelon, J., Totems, J., Chazette, P., Bazureau, A., Sicard, M., et al. (2016). Long-range transport and mixing of aerosol sources during the 2013 North American biomass burning episode: Analysis of multiple lidar observations in the western Mediterranean basin. *Atmospheric Chemistry and Physics*, *16*, 4725–4742. https://doi.org/10.5194/acp-16-4725-2016

Backus, G. E., & Gilbert, J. F. (1970). Uniqueness in the inversion of inaccurate gross Earth data. *Philosophical Transactions of the Royal Society of London, Series A: Mathematical, Physical and Engineering Sciences*, *266*, 123–192.

Bayes, T., & Price, R. (1763). An essay towards solving a problem in the doctrine of chance. By the late Rev. Mr. Bayes, communicated by Mr. Price, in a letter to John Canton, A. M. F. R. S. *Philosophical Transactions of the Royal Society of London*, *53*, 370–418. https://doi.org/10.1098/rstl.1763.0053

Bösch, T., Rozanov, V., Richter, A., Peters, E., Rozanov, A., Wittrock, F., et al. (2018). BOREAS—A new MAX-DOAS profile retrieval algorithm for aerosols and trace gases. *Atmospheric Measurement Techniques*, *11*, 6833–6859. https://doi.org/10.5194/amt-11-6833-2018

Bovensmann, H., Burrows, J. P., Buchwitz, M., Frerick, J., Noël, S., & Rozanov, V. (1999). SCIAMACHY: Mission objectives and measurement modes. *Journal of the Atmospheric Sciences*, *56*(2), 127–150.

Burrows, J. P., Weber, M., Buchwitz, M., Rozanov, V., Ladstätter-Weißenmayer, A., Richter, A., et al. (1999). The global ozone monitoring experiment (GOME): Mission concept and first scientific results. *Journal of the Atmospheric Sciences*, *56*, 151–175.

Carlton, A. G., Wiedinmyer, C., & Kroll, J. H. (2009). A review of secondary organic aerosol (SOA) formation from isoprene. *Atmospheric Chemistry and Physics*, *9*(14), 4987–5005. https://doi.org/10.5194/acp-9-4987-2009

Castro, T., Madronich, S., Rivale, S., Muhlia, A., & Mar, B. (2001). The influence of aerosols on photochemical smog in Mexico City. *Atmospheric Environment*, *25*, 1765–1772.

Chance, K., X. Liu, C. Chan Miller, G. González Abad, G. Huang, C. Nowlan, et al., 2019, TEMPO green paper: Chemistry, physics, and meteorology experiments with the tropospheric emissions: Monitoring of pollution instrument, Proc. SPIE 11151, sensors, systems, and next-generation satellites XXIII, 111510B, 2019., doi:https://doi.org/10.1117/12.2534883

Chang, D. Y., Lelieveld, J., Tost, H., Steil, B., Pozzer, A., & Yoon, J. (2017). Aerosol physicochemical effects on CCN activation simulated with the chemistry-climate model EMAC. *Atmospheric Environment*, *162*, 127–140. https://doi.org/10.1016/j.atmosenv.2017.03.036

Chen, Y., & Bond, T. C. (2010). Light absorption by organic carbon from wood combustion. *Atmospheric Chemistry and Physics*, *10*, 1773–1787.

Chimot, J., Vlemmix, T., Veefkind, J. P., de Haan, J. F., & Levelt, P. F. (2016). Impact of aerosols on the OMI tropospheric NO_2 retrievals over industrialized regions: How accurate is the aerosol correction of cloud-free scenes via a simple cloud model? *Atmospheric Measurement Techniques*, *9*(2), 359–382. https://doi.org/10.5194/amt-9-359-2016

Devaux, C., Vermeulen, A., Deuze, J. L., Dubuisson, P., Herman, M., & Santer, R. (1998). Retrieval of aerosol single-scattering albedo from ground-based measurements: Application to observational data. *Journal of Geophysical Research*, *103*, 8753–8761.

Dickerson, R. R., Kondragunta, S., Stenchikov, G., Civerolo, K. L., Doddridge, B. G., & Holben, B. N. (1997). The impact of aerosols on solar ultraviolet radiation and photochemical smog. *Science*, *278*(5339), 827–830. https://doi.org/10.1126/science.278.5339.827

Du, H., Kong, L., Cheng, T., Chen, J., Yang, X., Zhang, R., et al. (2010). Insights into ammonium particle-to-gas conversion: Non-sulfate ammonium coupling with nitrate and chloride. *Aerosol and Air Quality Research*, *10*, 589–595. https://doi.org/10.4209/aaqr.2010.04.0034

Dubovik, O., Holben, B. N., Kaufman, Y. J., Yamasoe, M., Smirnov, A., Tanré, D., & Slutsker, I. (1998). Single-scattering albedo of smoke retrieved from the sky radiance and solar transmittance measured from ground. *Journal of Geophysical Research*, *103*, 31,903–31,924.

Dubovik, O., & King, M. D. (2000). A flexible inversion algorithm for retrieval of aerosol optical properties from Sun and sky radiance measurements. *Journal of Geophysical Research*, *105*, 20,673–20,696. https://doi.org/10.1029/2000JD900282

Dubovik, O., Smirnov, A., Holben, B. N., King, M. D., Kaufman, Y. J., Eck, T. F., & Slutsker, I. (2000). Accuracy assessments of aerosol optical properties retrieved from Aerosol Robotic Network (AERONET) Sun and sky radiance measurements. *Journal of Geophysical Research*, *105*, 9791–9806.

Dusek, U., Frank, G. P., Hildebrandt, L., Curtius, J., Schneider, J., Walter, S., et al. (2006). Size matters more than chemistry for cloud-nucleating ability of aerosol particles. *Science*, *312*(5778), 1375–1378. https://doi.org/10.1126/science.1125261

Eck, T. F., Holben, B. N., Reid, J. S., Dubovik, O., Smirnov, A., O'Neill, N. T., et al. (1999). Wavelength dependence of the optical depth of biomass burning, urban, and desert dust aerosols. *Journal of Geophysical Research*, *104*(D24), 31,333–31,349. https://doi.org/10.1029/1999JD900923

Eck, T. F., Holben, B. N., Reid, J. S., Xian, P., Giles, D. M., Sinyuk, A., et al. (2018). Observations of the interaction and transport of fine mode aerosols with cloud and/or fog in Northeast Asia from aerosol robotic network and satellite remote sensing. *Journal of Geophysical Research – Atmospheres*, *123*, 5560–5587. https://doi.org/10.1029/2018JD028313

Eck, T. F., Holben, B. N., Sinyuk, A., Pinker, R. T., Goloub, P., Chen, H., et al. (2010). Climatological aspects of the optical properties of fine/coarse mode aerosol mixtures. *Journal of Geophysical Research*, *115*, D19205. https://doi.org/10.1029/2010JD014002

Facchini, M. C., Decesari, S., Mircea, M., Fuzzi, S., & Loglio, G. (2000). Surface tension of atmospheric wet aerosol and cloud/fog droplets in relation to their organic carbon content and chemical composition. *Atmospheric Environment*, *34*, 4853–4857.

Fairlie, T. D., Jacob, D. J., & Park, R. J. (2007). The impact of transpacific transport of mineral dust in the United States. *Atmospheric Environment*, *41*, 1251–1266. https://doi.org/10.1016/j.atmosenv.2006.09.048

Flores, J. M., Washenfelder, R. A., Adler, G., Lee, H. J., Segev, L., Laskin, J., et al. (2014). Complex refractive indices in the near-ultraviolet spectral region of biogenic secondary organic aerosol aged with ammonia. *Physical Chemistry Chemical Physics*, *16*, 10,629–10,642. https://doi.org/10.1039/c4cp01009d

Flores, J. M., Zhao, D. F., Segev, L., Schlag, P., Kiendler-Scharr, A., Fuchs, H., et al. (2014). Evolution of the complex refractive index in the UV spectral region in aging secondary organic aerosol. *Atmospheric Chemistry and Physics*, *14*, 5793–5806. https://doi.org/10.5194/acp-14-5793-2014

Frankenberg, C., Hasekamp, O., O'Dell, C., Sanghavi, S., Butz, A., & Worden, J. (2012). Aerosol information content analysis of multi-angle high spectral resolution measurements and its benefit for high accuracy greenhouse gas retrievals. *Atmospheric Measurement Techniques*, *5*(7), 1809–1821.

Frieß, U., Monks, P. S., Remedios, J. J., Rozanov, A., Sinreich, R., Wagner, T., & Platt, U. (2006). MAX-DOAS O_4 measurements: A new technique to derive information on atmospheric aerosols: 2. Modeling studies. *Journal of Geophysical Research*, *111*, D14203. https://doi.org/10.1029/2005JD006618

Gelaro, R., McCarty, W., Suárez, M. J., Todling, R., Molod, A., Takacs, L., et al. (2017). The Modern-Era Retrospective Analysis for Research And Applications, Version 2 (MERRA-2). *Bulletin of the American Meteorological Society*, *30*(13), 5419–5454. https://doi.org/10.1175/JCLI-D-16-0758.1

Giles, D. M., Holben, B. N., Tripathi, S. N., Eck, T. F., Newcomb, W. W., Slutsker, I., et al. (2011). Aerosol properties over the Indo-Gangetic Plain: A mesoscale perspective from the TIGERZ experiment. *Journal of Geophysical Research*, *116*, D18203. https://doi.org/10.1029/2011JD015809

Giles, D. M., Sinyuk, A., Sorokin, M. G., Schafer, J. S., Smirnov, A., Slutsker, I., et al. (2019). Advancements in the Aerosol Robotic Network (AERONET) Version 3 database—Automated near-real-time quality control algorithm with improved cloud screening for Sun photometer aerosol optical depth (AOD) measurements. *Atmospheric Measurement Techniques*, *12*, 169–209. https://doi.org/10.5194/amt-12-169-2019

Gillespie, J. B., & Lindberg, J. D. (1992). Ultraviolet and visible imaginary refractive-index of strongly absorbing atmospheric particulate matter. *Applied Optics*, *31*(12), 2112–2115. https://doi.org/10.1364/AO.31.002112

Guyon, P., Frank, G. P., Welling, M., Chand, D., Artaxo, P., Rizzo, L., et al. (2005). Airborne measurements of trace gas and aerosol particle emissions from biomass burning in Amazonia. *Atmospheric Chemistry and Physics*, *5*, 2989–3002. https://doi.org/10.5194/acp-5-2989-2005

Halthore, R. N., Crisp, D., Schwartz, S. E., Anderson, G. P., Berk, A., Bonnel, B., et al. (2005). Intercomparison of shortwave radiative transfer codes and measurements. *Journal of Geophysical Research*, *110*, D11206. https://doi.org/10.1029/2004JD005293

Hansell, R. A., Tsay, S.-C., Pantina, P., Lewis, J. R., Ji, Q., & Herman, J. R. (2014). Spectral derivative analysis of solar spectroradiometric measurements: Theoretical basis. *Journal of Geophysical Research – Atmospheres*, *119*, 8908–8924. https://doi.org/10.1002/2013JD021423

Hao, L., Romakkaniemi, S., Kortelainen, A., Jaatinen, A., Portin, H., Miettinen, P., et al. (2013). Aerosol chemical composition in cloud events by high resolution time-of-flight aerosol mass spectrometry. *Environmental Science & Technology*, *47*, 2645–2653. https://doi.org/10.1021/es302889w

He, S., & Carmichael, G. R. (1999). Sensitivity of photolysis rates and ozone production in the troposphere to aerosol properties. *Journal of Geophysical Research*, *104*, 26,307–26,324. https://doi.org/10.1029/1999JD900789

Herman, J., Abuhassan, N., Kim, J., Kim, J., Dubey, M., Raponi, M., & Tzortziou, M. (2019). Underestimation of column NO_2 amounts from the OMI satellite compared to diurnally varying ground-based retrievals from multiple PANDORA spectrometer instruments. *Atmospheric Measurement Techniques*, *12*, 5593–5612, https://doi.org/10.5194/amt-12-5593-2019.

Herman, J., Cede, A., Spinei, E., Mount, G., Tzortziou, M., & Abuhassan, N. (2009). NO_2 column amounts from ground-based Pandora and MFDOAS spectrometers using the direct-sun DOAS technique: Intercomparisons and application to OMI validation. *Journal of Geophysical Research*, *114*, D13307. https://doi.org/10.1029/2009JD011848

Herman, J., Evans, R., Cede, A., Abuhassan, N., Petropavlovskikh, I., & McConville, G. (2015). Comparison of ozone retrievals from the Pandora spectrometer system and Dobson spectrometer in Boulder, Colorado. *Atmospheric Measurement Techniques*, *8*, 3407–3418.

Hess, M., Koepke, P., & Schult, I. (1998). Optical properties of aerosols and clouds: The software package OPAC. *Bulletin of the American Meteorological Society*, *79*, 831–844.

Holben, B. N., Eck, T. F., Slutsker, I., Tanré, D., Buis, J. P., Setzer, A., et al. (1998). AERONET—A federated instrument network and data archive for aerosol characterization. *Remote Sensing of Environment*, *66*, 1–17. https://doi.org/10.1016/S0034-4257(98)00031-5

Holben, B. N., Tanré, D., Kaufman, Y., Slutsker, I., & Ward, D. (1996). Single-scattering albedo approximated from ground based measurements of aerosol optical thickness in the Amazon Basin. In V. Kirchoff (Ed.), *SCAR-B Proceedings*, (pp. 73–77). São Paulo, Brazil: Transtec Edit.

Hong, H., Lee, H., Kim, J., Jeong, U., Ryu, J., & Lee, D. S. (2017). Investigation of simultaneous effects of aerosol properties and aerosol peak height on the air mass factors for space-borne NO_2 retrievals. *Remote Sensing*, *9*(3), 208. https://doi.org/10.3390/rs9030208

Ingmann, P., Veihelmann, B., Langen, J., Lamarre, D., Stark, H., & Courreges-Lacoste, G. B. (2012). Requirements for the GMES atmosphere service and ESA's implementation concept: Sentinels-4/5 and -5p. *Remote Sensing of Environment*, *120*, 58–69. https://doi.org/10.1016/j.rse.2012.01.023

IPCC (Intergovernmental Panel on Climate Change) (2013). *Contribution of Working Group I to the Fifth Assessment Report of the Intergovernmental Panel on Climate Change*. Cambridge, UK and New York: Cambridge University Press.

Irie, H., Kanaya, Y., Akimoto, H., Iwabuchi, H., & Aoki, K. (2008). First retrieval of tropospheric aerosol profiles using MAX-DOAS and comparison with lidar and sky radiometer measurements. *Atmospheric Chemistry and Physics*, *8*, 341–350. https://doi.org/10.5194/acp-8-341-2008

Irie, H., Takashima, H., Kanaya, Y., Boersma, K. F., Gast, L., Wittrock, F., et al. (2011). Eight-component retrievals from ground-based MAX-DOAS observations. *Atmospheric Measurement Techniques*, *4*, 1027–1044. https://doi.org/10.5194/amt-4-1027-2011

Jaross, G., Bhartia, P. K., Chen, G., Kowitt, M., Haken, M., Chen, Z., et al. (2014). OMPS limb profiler instrument performance assessment. *Journal of Geophysical Research – Atmospheres*, *119*, 4399–4412. https://doi.org/10.1002/2013JD020482

Jeong, U., Kim, J., Ahn, C., Torres, O., Liu, X., Bhartia, P. K., et al. (2016). An optimal-estimation-based aerosol retrieval algorithm using OMI near-UV observations. *Atmospheric Chemistry and Physics*, *16*, 177–193. https://doi.org/10.5194/acp-16-177-2016

Jeong, U., Kim, J., Lee, H., & Lee, Y. G. (2017). Assessing the effect of long-range pollutant transportation on air quality in Seoul using the conditional potential source contribution function method. *Atmospheric Environment*, *150*, 33–44. https://doi.org/10.1016/j.atmosenv.2016.11.017

Jeong, U., Tsay, S.-C., Pantina, P., Butler, J. J., Loftus, A. M., Abuhassan, N., et al. (2018). Langley calibration analysis of solar spectroradiometric measurements: Spectral aerosol optical thickness retrievals. *Journal of Geophysical Research – Atmospheres*, *123*, 4221–4238. https://doi.org/10.1002/2017JD028262

Jin, Z., Charlock, T. P., Rutledge, K., Cota, G., Kahn, R., Redemann, J., et al. (2005). Radiative transfer modeling for the CLAMS experiment. *Journal of the Atmospheric Sciences*, *62*, 1053–1071.

Keyte, I. J., Harrison, R. M., & Lammel, G. (2013). Chemical reactivity and long-range transport potential of polycyclic aromatic hydrocarbons—A review. *Chemical Society Reviews*, *42*(24), 9333–9391. https://doi.org/10.1039/c3cs60147a

Kim, J., Jeong, U., Ahn, M.-H., Kim, J. H., Park, R. J., Lee, H., et al. (2019). New era of air quality monitoring from space: Geostationary Environment Monitoring Spectrometer (GEMS). *Bulletin of the American Meteorological Society*, *101*(1), E1–E22. https://doi.org/10.1175/BAMS-D-18-0013.1

Kirchstetter, T. W., Novakov, T., & Hobbs, P. V. (2004). Evidence that the spectral dependence of light absorption by aerosols is affected by organic carbon. *Journal of Geophysical Research*, *109*, D21208. https://doi.org/10.1029/2004JD004999

Kok, J. F. (2011). A scaling theory for the size distribution of emitted dust aerosols suggests climate models underestimate the size of the global dust cycle. *PNAS*, *108*(3), 1016–1021. https://doi.org/10.1073/pnas.1014798108

Levelt, P. F., van den Oord, G. H. J., Dobber, M. R., Mälkki, A., Visser, H., de Vries, J., et al. (2006). The ozone monitoring instrument. *IEEE Transactions on Geoscience and Remote Sensing*, *44*(5), 1093–1101.

Linak, W. P., Miller, C. A., Seames, W. S., Wendt, J., Ishinomori, T., Endo, Y., & Miyamae, S. (2002). On trimodal particle size distribution in fly ash from pulverized-coal combustion. *Proceedings of the Combustion Institute*, *29*, 441–447.

Mahowald, N., Albani, S., Kok, J. F., Engelstaeder, S., Scanza, R., Ward, D. S., & Flanner, M. G. (2014). The size distribution of desert dust aerosols and its impact on the Earth system. *Aeolian Research*, *15*, 53–71. https://doi.org/10.1016/j.aeolia.2013.09.002

Mahowald, N. M., Muhs, D. R., Levis, S., Rasch, P. J., Yoshioka, M., Zender, C. S., & Luo, C. (2006). Change in atmospheric mineral aerosols in response to climate: Last glacial period, preindustrial, modern, and doubled carbon dioxide climates. *Journal of Geophysical Research*, *111*, D10202. https://doi.org/10.1029/2005JD006653

Martins, J. V., Artaxo, P., Kaufman, Y. J., Castanho, A. D., & Remer, L. A. (2009). Spectral absorption properties of aerosol particles from 350-2500 nm. *Geophysical Research Letters*, *36*, L13810. https://doi.org/10.1020/2009GL037435

McMeeking, G. R., Bart, M., Chazette, P., Haywood, J. M., Hopkins, J. R., McQuaid, J. B., et al. (2012). Airborne measurements of trace gases and aerosols over the London metropolitan region. *Atmospheric Chemistry and Physics*, *12*, 5163–5187. https://doi.org/10.5194/acp-12-5163-2012

Meng, Z., Dabdub, D., & Seinfeld, J. H. (1997). Chemical coupling between atmospheric ozone and particulate matter. *Science*, *277*(5322), 116–119. https://doi.org/10.1126/science.277.5322.116

Menke, W. (1984). *Geophysical data analysis: Discrete inverse theory*. San Diego, CA: Academic Press.

Mishchenko, M. I., Zakharova, N. T., Videen, G., Khlebtsov, N. G., & Wriedt, T. (2010). Comprehensive T-matrix reference database: A 2007–2009 update. *Journal of Quantitative Spectroscopy and Radiative Transfer*, *111*, 650–658. https://doi.org/10.1016/j.jqsrt.2009.11.002

Mochida, M., Nshita-Hara, C., Furutani, H., Miyazaki, Y., Jung, J., Kawamura, K., & Uematsu, M. (2011). Hygroscopicity and cloud condensation nucleus activity of marine aerosol particles over the western North Pacific. *Journal of Geophysical Research*, *116*, D06204. https://doi.org/10.1029/2010JD014759

Mok, J., Krotkov, N. A., Arola, A., Torres, O., Jethva, H., Andrade, M., et al. (2016). Impacts of brown carbon from biomass burning on surface UV and ozone photochemistry in the Amazon Basin. *Science Report-UK*, *6*, 36940. https://doi.org/10.1038/srep36940

Mok, J., Krotkov, N. A., Torres, O., Jethva, H., Li, Z., Kim, J., et al. (2018). Comparisons of spectral aerosol single scattering albedo in Seoul, South Korea. *Atmospheric Measurement Techniques*, *11*, 2295–2311. https://doi.org/10.5194/amt-11-2295-2018

Munro, R., Lang, R., Klaes, D., Poli, G., Retscher, C., Lindstrot, R., et al. (2016). The GOME-2 instrument on the Metop series of satellites: Instrument design, calibration, and level 1 data processing-an overview. *Atmospheric Measurement Techniques*, *9*, 1279–1301.

Nakajima, T., Tanaka, M., & Yamauchi, T. (1983). Retrieval of the optical properties of aerosols from aureole and extinction data. *Applied Optics*, *22*, 2951–2959.

Nakajima, T., Tonna, G., Rao, R., Boi, P., Kaufman, Y., & Holben, B. N. (1996). Use of sky brightness measurements from ground for remote sensing of particulate polydispersions. *Applied Optics*, *35*, 2672–2686.

Ning, D.-T., Zhong, L.-X., & Chung, Y.-S. (1996). Aerosol size distribution and elemental composition in urban areas of northern China. *Atmospheric Environment*, *30*(13), 2355–2362.

Rodgers, C. D. (1990). Characterization and error analysis of profiles retrieved from remote sounding measurements. *Journal of Geophysical Research*, *95*, 5587–5595. https://doi.org/10.1029/JD095id05p05587

Rodgers, C. D. (1998). Information content and optimisation of high spectral resolution remote measurements. *Advances in Space Research*, *21*(3), 361–367.

Rodgers, C. D. (2000). *Inverse method for atmospheric sounding: Theory and practice, World Scientific Publishing co*. Singapore: Pte. Ltd.

Ryder, C. L., Highwood, E. J., Lai, T. M., Sodeman, H., & Masham, J. H. (2013). Impact of atmospheric transport on the evolution of microphysical and optical properties of Saharan dust. *Geophysical Research Letters*, *40*, 2433–2438. https://doi.org/10.1002/grl.50482

Saleh, R., Hennigan, C. J., McMeeking, G. R., Chuang, W. K., Robinson, E. S., Coe, H., et al. (2013). Absorptivity of brown carbon in fresh and photo-chemically aged biomass-burning emissions. *Atmospheric Chemistry and Physics*, *13*, 7683–7693. https://doi.org/10.5194/acp-13-7683-2013

Sanghavi, S., Martonchik, J. V., Landgraf, J., & Platt, U. (2012). Retrieval of the optical depth and vertical distribution of particulate scatterers in the atmosphere using O2 A- and B-band SCIAMACHY observations over Kanpur: A case study. *Atmospheric Measurement Techniques*, *5*, 1099–1119. https://doi.org/10.5194/amt-5-1099-2012

Schauer, J. J., & Cass, G. R. (2000). Source apportionment of wintertime gas-phase and particle phase air pollutants using organic compounds as tracers. *Environmental Science & Technology*, *34*, 1821–1832. https://doi.org/10.1021/es981312t

Schmale, J., Henning, S., Decesari, S., Henzing, B., Keskinen, H., Sellegri, K., et al. (2018). Long-term cloud condensation nuclei number concentration, particle number size distribution and chemical composition measurements at regionally representative observations. *Atmospheric Chemistry and Physics*, *18*(4), 2853–2881. https://doi.org/10.5194/acp-18-2853-2018

Seftor, C. J., Jaross, G., Kowitt, M., Haken, M., Li, J., & Flynn, L. E. (2014). Postlaunch performance of the Suomi National Polar-orbiting Partnership Ozone Mapping and Profiler Suite (OMPS) nadir sensors. *Journal of Geophysical Research – Atmospheres*, *119*, 4413–4428. https://doi.org/10.1002/2013JD020472

Sentenac, T., Maoultt, Y. L., Rolland, G., & Devy, M. (2003). Temperature correction of radiometric and geometric models for and uncooled CCD camera in the near infrared. *IEEE Transactions on Instrumentation and Measurement*, *52*(1), 46–60. https://doi.org/10.1109/TIM.2003.809103

Shepherd, R. H., King, M. D., Marks, A. A., Brough, N., & Ward, A. D. (2018). Determination of the refractive index of insoluble organic extracts from atmospheric aerosol over the visible wavelength range using optical tweezers. *Atmospheric Chemistry and Physics*, *18*, 5235–5252. https://doi.org/10.5194/acp-18-5235-2018

Sinyuk, A., Holben, B. N., Eck, T. F., Giles, D. M., Slutsker, I., Korkin, S., et al. (2020). The AERONET version 3 aerosol retrieval algorithm, associated uncertainties and comparisons to version 2. *Atmospheric Measurement Techniques Discussions*. https://doi.org/10.5194/amt-2019-474

Sokolik, I. N., & Toon, O. B. (1999). Incorporation of mineralogical composition into models of the radiative properties of mineral aerosol from UV to IR wavelengths. *Journal of Geophysical Research*, *104*, 9423–9444. https://doi.org/10.1029/1998JD200048

Spurr, R. J. D. (2006). VLIDORT: A linearized pseudo-spherical vector discrete ordinate radiative transfer code for forward model and retrieval studies in multilayer multiple scattering media. *Journal of Quantitative Spectroscopy and Radiative Transfer*, *102*, 316–342. https://doi.org/10.1016/j.jqsrt.2006.05.005

Spurr, R. J. D., & Christi, M. (2014). On the generation of atmospheric property Jacobians from the (V)LIDORT linearized radiative transfer models. *Journal of Quantitative Spectroscopy and Radiative Transfer*, *142*, 109–115. https://doi.org/10.1016/j.jqsrt.2014.03.011

Spurr, R. J. D., Wang, J., Zeng, J., & Mishchenko, M. I. (2012). Linearized T-matrix and Mie scattering computations. *Journal of Quantitative Spectroscopy and Radiative Transfer*, *113*, 425–439. https://doi.org/10.1016/j.jqsrt.2011.11.014

Stamnes, K., Tsay, S.-C., Wiscombe, W. J., & Jayaweera, K. (1988). Numerically stable algorithm for discrete-ordinate-method radiative transfer in multiple scattering and emitting layered media. *Applied Optics*, *27*, 2,502–2,509.

Stockwell, C. E., Jayarathne, T., Cochrane, M. A., Ryan, K. C., Putra, E. I., Saharjo, B. H., et al. (2016). Field measurements of trace gases and aerosols emitted by peat fires in Central Kalimantan, Indonesia, during the 2015 El Niño. *Atmospheric Chemistry and Physics*, *16*, 11,711–11,732. https://doi.org/10.5194/acp-16-11711-2016

Szykman, J., Swap, R. J., Lefer, B., Valin, L., Lee, S. C., Fioletov, V., et al., (2019). Pandora: Connecting in-situ and satellite monitoring in support of the Canada-U.S. Air quality agreement, EM: Air and waste management Association's magazine for environmental managers.

Torres, O., Tanskanen, A., Veihelmann, B., Ahn, C., Braak, R., Bhartia, P. K., et al. (2007). Aerosols and surface UV products from Ozone Monitoring Instrument observations: An overview. *Journal of Geophysical Research*, *112*, D24S47. https://doi.org/10.1029/2007JD008809

Tsay, S.-C., Maring, H. B., Lin, N.-H., Buntoung, S., Chantara, S., Chuang, H.-C., et al. (2016). Satellite-surface perspectives of air quality and aerosol-cloud effects on the environment: An overview of 7-SEAS/BASELInE. *Aerosol and Air Quality Research*, *16*, 2581–2602. https://doi.org/10.4209/aaqr.2016.08.0350

Väisänen, O., Ruuskanen, A., Ylisirniö, A., Miettinen, P., Portin, H., Hao, L., et al. (2016). In-cloud measurements highlight the role of aerosol hygroscopicity in cloud droplet formation. *Atmospheric Chemistry and Physics*, *16*, 10,385–10,398. https://doi.org/10.5194/acp-16-10385-2016

van Geffen, J. H. G. M. (2004). Wavelength calibration of spectra measured by the global ozone monitoring experiment: Variations along orbits and in time. *Applied Optics*, *43*(3), 695–706. https://doi.org/10.1364/AO.43.000695

van Weele, M., Martin, T. J., Blumthaler, M., Brogniez, C., den Outer, P. N., Engelsen, O., et al. (2000). From model intercomparison toward benchmark UV spectra for six real atmospheric cases. *Journal of Geophysical Research*, *105*(D4), 4915–4925.

Vieno, M., Heal, M. R., Hallsworth, S., Famulari, D., Doherty, R. M., Dore, A. J., et al. (2014). The role of long-range transport and domestic emissions in determining atmospheric secondary inorganic particle concentrations across the UK. *Atmospheric Chemistry and Physics*, *14*, 8435–8447. https://doi.org/10.5194/acp-14-8435-2014

Wagner, T., Dix, B., Friedeburg, C. V., Frieß, U., Sanghavi, S., Sinreich, R., & Platt, U. (2004). MAX-DOAS O_4 measurements: A new technique to derive information on atmospheric aerosols – Principles and information content. *Journal of Geophysical Research*, *109*, D22205. https://doi.org/10.1029/2004JD004904

Washenfelder, R. A., Flores, J. M., Brock, C. A., Brown, S. S., & Rudich, Y. (2013). Broadband measurements of aerosol extinction in the ultraviolet spectral region. *Atmospheric Measurement Techniques*, *6*, 861–877. https://doi.org/10.5194/amt-6-861-2013

Welton, E. J., Campbell, J. R., Spinhirne, J. D., & Scott, V. S. (2001). Global monitoring of clouds and aerosols using a network of Micro-pulse Lidar systems. In U. N. Singh, T. Itabe, & N. Sugimoto (Eds.), *Lidar remote sensing for industry and environmental monitoring*, *Proc. SPIE* (Vol. 4153, pp. 151–158). https://doi.org/10.1117/12.417040

Xu, X., & Wang, J. (2015). Retrieval of aerosol microphysical properties from AERONET photopolarimetric measurements: 1. Information content analysis. *Journal of Geophysical Research: Atmosphere*, *120*, 7059–7078. https://doi.org/10.1002/2015JD023108

Yang, P., Feng, Q., Hong, G., Kattawar, G. W., Wiscombe, W. J., Mishchenko, M. I., et al. (2007). Modeling of the scattering and radiative properties of nonspherical dust-like aerosols. *Journal of Aerosol Science*, *38*, 995–1014. https://doi.org/10.1016/j.jaerosci.2007.07.001

Zelenyuk, A., Imre, D., Beránek, J., Abramson, E., Wilson, J., & Shrivastava, M. (2012). Synergy between secondary organic aerosols and long-range transport of polycyclic aromatic hydrocarbons. *Environmental Science & Technology*, *46*, 12,459–12,466. https://doi.org/10.1021/es302743z

Zhang, L., Gong, S., Padro, J., & Barrie, L. (2001). A size-segregated particle dry deposition scheme for an atmospheric aerosol module. *Atmospheric Environment*, *35*(3), 549–560. https://doi.org/10.1016/S1352-2310(00)00326-5

Zhang, L., Kok, J. F., Henze, D. K., Li, Q., & Zhao, C. (2013). Improving simulations of fine dust surface concentrations over the western United States by optimizing the particle size distribution. *Geophysical Research Letters*, *40*, 3270–3275. https://doi.org/10.1002/grl.50591

Zhang, R., Wang, G., Guo, S., Zamora, M. L., Ying, Q., Lin, Y., et al. (2015). Formation of urban fine particulate matter. *Chemical Reviews*, *115*, 3803–3855. https://doi.org/10.1021/acs.chemrev.5b00067

Zhang, Y., Li, Z., Zhang, Y., Li, D., Qie, L., Che, H., & Xu, H. (2017). Estimation of aerosol complex refractive indices for both fine and coarse modes simultaneously based on AERONET remote sensing products. *Atmospheric Measurement Techniques*, *10*, 3203–3213. https://doi.org/10.5194/amt-10-3203-2017

Zhong, M., & Jang, M. (2014). Dynamic light absorption of biomass-burning organic carbon photochemically aged under natural sunlight. *Atmospheric Chemistry and Physics*, *14*, 1517–1525. https://doi.org/10.5194/acp-14-1517-2014

Ziemann, P. J., & Atkinson, R. (2012). Kinetics, products, and mechanisms of secondary organic aerosol formation. *Chemical Society Reviews*, *41*(19), 6582–6605. https://doi.org/10.1039/c2cs35122f

Zoogman, P., Liu, X., Suleiman, R. M., Pennington, W. F., Flittner, D. E., Al-Saadi, J. A., et al. (2017). Tropospheric emissions: Monitoring of pollution (TEMPO). *Journal of Quantitative Spectroscopy and Radiative Transfer*, *186*, 17–39. https://doi.org/10.1016/jqsrt.2016.05.008